Characterizing T_2 Distributions in Healthy White Matter.

by

Bretta Adrianne Russell-Schulz

BSc (Hons), University of Newfoundland, 2009

A THESIS SUBMITTED IN PARTIAL FULFILLMENT
OF THE REQUIREMENTS FOR THE DEGREE OF

Master of Science

in

THE FACULTY OF GRADUATE STUDIES
(Physics)

The University Of British Columbia
(Vancouver)

October 2011

Abstract

Quantitative T_2 measurements in magnetic resonance imaging (MRI) can provide information about water environments in biological structures. Here, an extended Carr-Purcell-Meiboom-Gill sequence (CPMG) with echoes out to $1120ms$ was used to characterize Long-T_2 times of healthy white matter in brain. One of the white matter structures, the corticospinal tract (CST), was previously found to be bright on T_2-weighted images and myelin water fraction (MWF) images. The intra-/extracellular water (IE) T_2 peak of the CST was found to be broadened in comparison to that from other white matter structures and often split into two distinct peaks. In the CST, it appeared that the intracellular and extracellular water environments had different T_2 times, causing the intracellular water peak to be pushed down into the myelin water T_2 regime and the extracellular peak to be pushed up to higher T_2 times. The conventional T_2 limits of $10-40ms$ used for the MWF at $1.5T$ result in an artificial increase in MWF, which causes the CST to be bright on myelin water images. When the upper limit of the MWF range was decreased to $25ms$, the CST exhibited MWF values similar to those found for adjacent anterior and posterior regions.

Using T_2 time of $25ms$ for the myelin water (MW) upper limit and IE lower limit, a moderately strong relationship between IE geometric mean T_2 (GMT_2) and MW was found across all structures and subjects. This relationship did not necessarily hold when examined across subjects within individual structures The relationship between IE GMT_2 and MWF could arise from a non-biological source, such as the algorithm used in calculating T_2 or from a biological source, such as exchange between the water environments or increased extracellular water. Based on our results the fitting algorithm does not appear to be responsible for this relationship

based on our results. However, either varying amounts of extracellular water or exchange between MW and IE could explain this relationship.

Preface

Two chapters of this thesis will be submitted for publication; Chapter 4: Russell-Schulz BA, Laule C, Li D, MacKay AL and Chapter 5: Russell-Schulz BA, Whittall K, Laule C, Li D, Prasloski T, MacKay AL.

Research Ethics

Ethics approval was obtained by Dr. Sandra Sirrs for the "Comparison of brain magnetic resonance spectroscopy with measurement of brain myelin content in individuals with cognitive deficits related to phenylketonuria" study. The Ethics Approval Code from the Clinical Research Ethics Board is C00-0235.

Identification and Design of the Research Program

I participated in discussion of the research goals and subsequent modifications to the research direction. The research protocol was developed by Sirrs et al. [58], the control protocol for T_2 data analysis was used for this thesis.

Performance of Research

The data came from a control group used for a study of phenylketonuria (PKU) [58], the research was funded by the Vancouver General Hospital and Health Sciences Centre Interdisciplinary Grant.

Data Analysis

I drew all the Regions of Interest (ROIS) with constructive input from Li D and Laule C. I performed all data analysis on these ROIS using a program created by Bjarnason TA (he also created the regularization and non-regularization code), except for the creation of the T_2 simulation. The code for the T_2 simulation was written by Prakloski T, I ran the simulations and completed all analysis of the simulation data. I completed all other data analysis including the statistical analysis.

Preparation of Manuscripts

I prepared the manuscript figures and text with the guidance and input from my co-authors.

Table of Contents

List of Tables

List of Figures

List of abbreviations

AIC anterior internal capsule

ALS amyotrophic lateral sclerosis

CC corpus callosum

CNS central nervous system

CPMG Carr-Purcell-Meiboom-Gill sequence, spin echo sequence used to measure T_2

CSF cerebrospinal fluid

CST corticospinal tract

DTI diffusion tensor imaging

GMT$_2$ geometric mean T_2

IC internal capsule

IE intra-/extra-cellular water, water between axons (extracellular) and water within the axons (intracellular)

IEF intra-/extra-cellular water fraction, the area under the IE T_2 peak over the total T_2 area

LT$_2$F Long-T_2 fraction

MR magnetic resonance

MRI magnetic resonance imaging

MS multiple sclerosis

MTR magnetization transfer ratio

MW myelin water, water between the myelin sheaths

MWF myelin water fraction, a measure that reflects myelin density

NMR nuclear magnetic resonance

NNLS non-negative least squares

PKU phenylketonuria

PL posterior limb

ROI Region of Interest

ROIS Regions of Interest

SNR signal-to-noise-ratio

TE echo time

TR repetition time, time between successive pulses in the same slice

W distribution width

Acknowledgments

I am grateful to all those who helped me in writing this thesis and in put up with my general frenzied state. I would like to give a special thanks for my friends and colleagues in M10 and G33 who were always willing to provide helpful input and specifically to Dr. Alex MacKay for his guidance and time. I would also like to thank my family and friends who have always been supportive not only through my school but also through my life.

Finally, completing this work would not have been possible without the support of Matthew, who not only put up with my 3am writing spurts but also provided me with many homemade meals and hot cups of tea. Thank you.

Dedication

To my mother, who I know would have been proud.

Chapter 1

Introduction

An important tool used to non-invasively examine the body is magnetic resonance imaging (MRI), it is particularly useful in examining the brain and associated pathologies such as multiple sclerosis (MS) [40]. Determining the magnetic resonance (MR) characteristics of healthy tissue is important for proper differentiation between it and pathological tissue. Quantitative T_2 relaxation and examination of the T_2 distributions of healthy tissue provides information that could be used to compare to pathological tissue [32, 35].

1.1 MRI and Brain Biochemistry

The brain is comprised mostly of water, resulting in a high presence of protons (hydrogen nuclei), which allows the brain to be well imaged using MRI. MRI is able to detect protons in different water environments and non-invasively produce images that can display brain anatomy and pathology. The water environment in which protons are found will have an effect on how the proton will react in the presence of a magnetic field and, as a result, different water environments will produce different signals in an MRI. Differences in water environment and the amount of water in different regions of the brain will provide contrast between these regions in a conventional MRI.

If the brain was comprised only of water it would appear as one bright region on an MRI with no contrast. However, the brain does not have a homogenous water

environment; the brain is made up of many different cells and structures, all of which will affect the signal detected in MRI in a different way. MRI can distinguish between white matter and grey matter in the brain due to the differences in the amounts of water and water environment depending on the type of image being produced.

The main distinction between white matter and grey matter is the high prevalence of myelin surrounding the white matter axons. Myelin is a protein-lipid bilayer that is wrapped in concentric circles around axons [33, 51, 52, 57]; the high lipid content in myelin is responsible for the white-ness of white matter [57]. Myelin provides insulation to the enclosed axons allowing for faster signal conduction [33, 51, 54, 57]. The size of the axon also has an influence on the speed of signal conduction; larger diameter axons are able to send signals faster than smaller diameter axons and have thicker myelin sheaths [55]. In general, the information in the brain that needs to be processed very quickly is sent along large myelinated axons [57]. Myelin composition is about $\sim 80\%$ lipids and $\sim 20\%$ proteins [33, 48, 51, 52] and in between the wrapped lipid-protein bilayers there is water, which accounts for approximately 40% of myelin's wet weight [12]. With conventional MRI sequences the protons on lipids and other non-water molecules are usually undetectable; this is due to the fact that the signal arising from these protons decay too quickly [7]. As a result, the signal measured from white matter is exclusively from water, and all water in the central nervous system (CNS) is thought to be measurable using MRI [13, 38]. Since directly measuring the signal from the myelin sheath is difficult, MRI techniques that measure the amount of myelin water, which should be a reflection of myelin content, have been developed [33].

The signal from white matter is a combination of the signal the from all the different water environments. This signal can be analyzed in such a way that the amount of each water environment can be separately determined (this technique will be described in Section 2.3). An important MRI concept is relaxation of the MRI signal; relaxation is responsible for much of the contrast on conventional MRI and can be used to identify pathological tissue, such as lesions in MS [40]. Relaxation is based on the inherent nature of the protons in a magnetic field to return to thermal equilibrium after being displaced. There are two types of relaxation: T_1,

which characterizes the return of the protons to a Boltzmann population aligned along the direction of $\mathbf{B_0}$; and T_2, which is the time it takes for the signal to decay. T_2 is called the spin-spin relaxation and is influenced by the surrounding 'spins', or the protons and molecules in its vicinity and the general motion of the protons (Brownian motion) [39]. The proximity of the proton to non-aqueous protons increases the decay of the proton's signal; protons closer to lipid bilayers would have shorter T_1 and T_2 decay time [40].

A T_2 distribution can be created by plotting the amplitude of the signal arising from different water environments against their respective T_2 times. This distribution can provide information about the different water environments; the area underneath the peak is a reflection of the amount of protons in each environment and the width and location of the peaks can provide additional information about the homogeneity [62]. While the amount of water in each environment is important, it is not the only information that can be useful in comparing healthy tissue to pathological tissue [34, 35] and in comparing among different healthy white matter structures [70].

1.2 Myelin Water Imaging

In theory, if only the water signal is being measured, the total signal from all these different water environments can be summed and when corrected with an external water source can be used to calculate the total water content of the brain [70]. In order to measure different water environments, which give rise to a multi-exponential signal decay, a 32-echo sequence was applied by MacKay et al. [38] to sample a large range of echo time (TE) times enabling the detection of shorter and longer T_2 times. The water content of white matter as measured by Whittall et al. [70] using the MacKay et al. [38] technique was similar to that measured in tissues using wet lab techniques [2, 11, 26, 49, 56, 63–65], adding further support for this technique as a measure of all water in the brain. Since all the water in the brain is detectable and there is a high prevalence of water between myelin sheaths, the water between sheaths or myelin water (MW) should be measurable.

In white matter T_2 relaxation experiments at least two different water environments have been detected; one arising from intra-/extra-cellular water (IE), which

is the water within an axon, the water between axons, and the water in glial cells; and another faster decaying T_2 component which has been identified as the water between myelin sheaths [38, 42–44, 62, 70]. This shorter T_2 component around $\sim 20ms$ had been assigned as MW in several *in vitro* studies [13, 42, 62, 66] before being detected *in vivo* [38].

Myelin content is determined by measuring the amount of myelin water signal, as a fraction of the total water signal, has been called myelin water fraction (MWF) and has been shown to be similar to the expected MWF of the white matter when calculated from histological myelin contents [30]. The MWF has also been shown to be proportional to the myelin content as estimated by histology [15, 16, 31, 36, 46, 67] and decreases in known myelin degenerated areas [30, 40].

1.3 Research Goals

The purpose of this work was to better characterize healthy white matter using a multi-exponential T_2 decay analysis with an extended Carr-Purcell-Meiboom-Gill sequence (CPMG) sequence that is used to better examine longer T_2 times [59]. The corticospinal tract (CST) was found to have a unique T_2 distribution for healthy white matter, which included signal at longer T_2 times but was not quantitatively compared to other white matter structures [35]. A proper understanding of 'normal' T_2 characteristics can help to distinguish it from pathological tissue. Healthy white matter T_2 distributions have not been compared using a sequence that allows proper characterization of longer T_2 times, this is important since longer T_2 times are often associated with pathology [34, 35].

The relationships between two different quantitative MR measures, MWF and location of the IE peak in health white matter were also explored. This relationship may provide additional information about the underlying physical characteristics of tissue. Possible relationships arising from experimental data must also be examined for non-physical influences, such as analysis techniques. Without proper examination of techniques used, the meaning of certain relationships cannot be considered to be real 'physical' relationships and this may lead to incorrect assumptions.

The full extent of the information available from examination of a T_2 relax-

ation in biological systems is not known. The purpose of this work is to expand on the current information available for 'normal' healthy white matter specifically using T_2 relaxation and to examine several possible outside non-physical influences. The first step in determining whether tissue is abnormal and possibly arising from pathology is to determine the properties of normal tissue.

Chapter 2

Background

2.1 NMR

The phenomenon of nuclear magnetic resonance (NMR) occurs in nuclei with spins (quantum number s) greater than zero when in the presence of an external magnetic field, $\mathbf{B_0}$. A nucleus with $s > 0$ also has an angular momentum, $\mathbf{J}$, and a magnetic moment, μ, which are non-zero. They are related by the following equation

$$\mu = \gamma \mathbf{J} \tag{2.1}$$

where γ is the gyromagnetic ratio, which is dependent on the nucleus state and is determined by finding the $\mathbf{J}$ and μ of a nucleus in a given magnetic field [60]. In the presence of $\mathbf{B_0}$, μ will line itself up with $\mathbf{B_0}$. If another magnetic field, $\mathbf{B_1}$ is applied at the resonant frequency of the system, μ will be tipped away from $\mathbf{B_0}$ and will precess around the direction of $\mathbf{B_0}$ [20]. It will precess with an angular frequency called the Larmor (the resonant frequency) determined by the Larmor equation which is given below

$$\omega_0 = \gamma B_0. \tag{2.2}$$

The most common NMR nucleus is hydrogen, ^1H, which has an $s = 1/2$ and therefore will be found in a superposition of the spin-up, $s = +\frac{1}{2}$ or spin-down, $s = -\frac{1}{2}$ state. When placed in $\mathbf{B}_0$, μ interacts with $\mathbf{B_0}$ and the hydrogen nucleus will have energy, which is dependent on its state (spin-up vs. spin-down). The

energy difference between the two spins states is found to be

$$\Delta E = \gamma \hbar B_0 \tag{2.3}$$

where $\hbar$ is the reduced Planck constant [60]. The energy difference is small, however, when a bulk of hydrogen nuclei are placed in $\mathbf{B_0}$ they will have a small preference to align themselves parallel and anti-parallel to the field. Using the Boltzmann distribution probability, it is found that there is a difference between the number of spins in each state due to the energy difference. This causes a net total $\mathbf{J}$ and magnetization, $\mathbf{M}$, in the direction of $\mathbf{B_0}$; the net magnetization of bulk nuclei, $\mathbf{M_0}$, allows for detectable NMR signal. If $\mathbf{M_0}$ is now tipped by $\mathbf{B_1}$ the nuclei will precess as dictated by Equation 2.2 [5]. The moving nuclei will induce a torque, which is the rate of change of $\mathbf{J}$. The equation of motion for the bulk nuclei becomes

$$\frac{d\mathbf{M}}{dt} = \gamma \mathbf{M} \times \mathbf{B}. \tag{2.4}$$

Equation 2.4 was determined using classical mechanics; the same solution can be obtained using quantum mechanics [60, 72]. The precession of $\mathbf{M}$ produces a signal that can be detected through Faraday's induction in an NMR receiver coil. Precession will not continue forever as given in Equation 2.4, the nuclei will instead return to thermal equilibrium ($\mathbf{M_0} \| \mathbf{B_0}$) through a process called relaxation.

It is convention in NMR to use a frame of reference rotating at the Larmor frequency denoted as x', y', z' [20, 72]. Thus, the changes to $\mathbf{M}$ are due to relaxation and $\mathbf{B_1}$. As stated before, $\mathbf{B_1}$ must also be rotating at ω_0, which tips $\mathbf{M}_0$ away from $\mathbf{B_0}$ through an angle α given by

$$\Delta\theta = \gamma B_1 \tau \tag{2.5}$$

where τ is the duration of the $\mathbf{B_1}$ field [5, 20, 72].

2.1.1 Relaxation

When $\mathbf{M}(t)$ is tipped away from equilibrium (z') by a radio frequency pulse there is now $\mathbf{M}(t)$ in x' and y' direction. After $\mathbf{B_1}$ is turned off $\mathbf{M}(t)$ in the z'-direction or

longitudinal magnetization ($\mathbf{M}_{\parallel}(t)$) will grow as $\mathbf{M}(t)$ returns to equilibrium and the x', y' component or transverse magnetization ($\mathbf{M}_{\perp}(t)$) will decay. The magnetization equation becomes

$$\frac{d\mathbf{M}(t)}{dt} = -\frac{M_x\hat{x} + M_y\hat{y}}{T_2} - \frac{(M_z - M_0)\hat{z}}{T_1} \tag{2.6}$$

where M_0 is the initial magnetization in $\hat{z}'$, and T_1 and T_2 are the longitudinal and transverse relaxation times respectively [72]. T_1 characterizes the time it takes to return to Boltzmann equilibrium along $\hat{z}'$ and T_2 characterizes the time it takes for the transverse magnetization to dephase. Assuming that initially $M_z = M_0$ and solving Equation 2.6, the longitudinal magnetization grows as

$$\mathbf{M}_{\parallel}(t) = M_0(1 - e^{-\frac{t}{T_1}}) \tag{2.7}$$

and the transverse magnetization decays as

$$\mathbf{M}_{\perp}(t) = \mathbf{M}_{\perp}(0)e^{-\frac{t}{T_2}} \tag{2.8}$$

where $\mathbf{M}_{\perp} = M_x\hat{x}' + M_y\hat{y}'$ [20, 60]. T_2 is also called the spin-spin relaxation time as the decay is due to the interactions between different spins. These interactions are due to the Brownian motion of molecules which produces fluctuating magnetic fields, causing dephasing and decay of the T_2 signal [6, 40]. Energy is conserved in this relaxation process and the signal is non-recoverable. The opposite is true for the T_1 relaxation process where energy is not conserved and the magnetization is recoverable [40].

2.1.2 T_2 Measurement

The T_2 being measured in Equation 2.8 is for an ideal system. However, in real experiments the T_2 decays at a faster rate and what would be measured in Equation 2.8 is designated as $T_2^{\star}$ [20]. Part of the $T_2^{\star}$ magnetization is recoverable, T_2', which arises from B field inhomogeneities. In order to measure the real T_2 time a pulse sequence like a spin-echo, such as a CPMG needs to be used [41]. A CPMG involves a 90° pulse around the x' axis, this brings all the magnetization into the

transverse plane. The signal dephases due to the B inhomogeneities and the spins spread out in the $x'y'$-plane during some elapsed time τ. At τ an 180° pulse applied which flips the spins and causes them to rephase along $+y'$ axis, in this way the signal lost to the B inhomogeneities is recovered at a time 2τ. At 2τ what is called an echo is formed. If the 180° pulse is repeated at times $n\tau$, where n is a non-negative integer, the intensity of the resulting echoes can be used to measure the real T_2 using the following equation,

$$S(TE) = S(TE = 0)e^{-\frac{TE}{T_2}} \tag{2.9}$$

where TE is the time where the echo occurs [20, 60, 72]. The output signal can be plotted on an amplitude verses $\log TE$ time curve that can be fit with an exponential equation to extract the real T_2 times. This will be further discussed in Section 2.3.

2.2 MRI

MRI is NMR with extra localization steps, which allow the creation of images, and is particularly good for tissue contrast in anatomy. This is achieved by the application of another **B**, which varies on top of $\mathbf{B_0}$, that is called a gradient, **G** and is defined by

$$\mathbf{G} = i\frac{\delta B_z}{\delta x} + j\frac{\delta B_z}{\delta y} + k\frac{\delta B_z}{\delta z}. \tag{2.10}$$

As a result of Equation 2.2 the Larmor frequency will also vary in space. In the z-direction the magnetic field would then be represented by [72]

$$\mathbf{B}_z(\mathbf{r},t) = \mathbf{B}_0 + \mathbf{r}\cdot\mathbf{G}(t) \tag{2.11}$$

where **r** is the position of the area being excited [20]. By encoding different areas of a sample with different Larmor frequencies the location can be determined or one area can be excited by the RF pulse, allowing for an image to be produced [72].

2.3 MRI in the Central Nervous System

In pure water the resultant decay curve from a CPMG can be fit using Equation 2.9 and thus appears as a straight line on a semi-log decay plot of signal vs. TE time. In

the brain, however, the water environment is inhomogeneous; it contains many different molecules in different water environments, this affects MRI results. In white matter, the decay curve does not follow a straight line, it is made up of different exponential decays from different water environments and is better represented by the following equation

$$S(TE) = \sum S_i e^{\frac{-TE}{T_{2i}}} \tag{2.12}$$

where T_{2i} is the T_2 time associated with different water environments i [40]. To properly characterize the different water environments with a range of T_2s, many echoes at different TEs should be used. A 32-echo sequence was applied by MacKay et al. [38] to image the brain at 1.5T and obtain T_2 decay curves. Not only is a proper sequence needed but also a proper fitting technique; this has been discussed and examined elsewhere [40]. A common technique used is a non-negative least squares (NNLS) fitting [37] which turns the decay curve into a distribution plot with amplitude of signal verses T_2 time. The different water environments appear as peaks on this distribution. A general form of the multi-exponential decay curve can be given as [39, 69]

$$y_i = \sum_{j=1}^{M} s(T_{2j}) e^{-\frac{t_i}{T_{2j}}} + \varepsilon_i, \qquad i = 1, 2, \cdots, N \tag{2.13}$$

where N is the number of measurements at time t_i, T_{2j} are the times of the water components, j, and $s(T_{2j})$ is the amplitude of these components. By splitting the T_2 spectrum into M summed δ functions the spectrum can be computed, where the spectrum is logarithmically partitioned into M T_2s, represented by T_{2j}. The term ε_i accounts for the noise associated with each point i. The NNLS fitting program minimizes the following terms

$$\chi^2 + \mu \sum_{j=1}^{M} s(T_{2j})^2, \qquad \mu \geqslant 0. \tag{2.14}$$

where χ^2 is the degree of misfit. The second term is called the regularizer, this constrains the system, μ is the regularization factor and sum of $s(T_{sj})^2$ over j components is the energy of the distribution. This factor smoothes discrete spike peaks into curves as μ is increased from 0, the curved peaks are more robust to

noise. Since the true χ^2_{min} would result from $\mu = 0$ producing discrete spikes, μ is increased to obtain a new fit by minimizing Equation 2.14 using the following constraints

$$1.02\chi^2_{min} \leqslant \chi^2 \leqslant 1.025\chi^2_{min} \tag{2.15}$$

in order to create smooth, rounded T_2 peaks [69].

2.4 Exchange

The exchange between two water environments can be important in MR measurements. Exchange is due to the movement of water protons from one environment (phase) to another where their relaxation will be different. The phase change of these protons, which is mostly due to diffusion in the brain, has an effect on the relaxation times . Exchange can cause an increase in the dephasing of the T_2 signal and therefore cause a decrease in the apparent T_2 of the pool being measured; the lifetime of the T_2 signal is thus artificially decreased [74]. If the exchange time is long on the timescale of the experiment then the exchange is considered too slow to affect the decay times. The signal can then be separated into different water environments with their own distinct characteristic decay times. However, if exchange is fast on the timescale of the experiment the T_2 time measured will be a combination of the different pools and cannot be accurately separated into components. The following derivation is taken from Zimmerman and Brittin [74] and Edzes and Samulski [10]. A modified Bloch equation can be used to describe the z magnetization in the presence of exchange of a two-pool water model as

$$\begin{gathered} \frac{d\mathbf{m}(t)}{dt} = -\mathbf{A}\mathbf{m}(t) \\ \mathbf{A} = \begin{bmatrix} \frac{1}{T_{2i}} + k_i & -k_i \\ -k_j & \frac{1}{T_{2j}} + k_j \end{bmatrix} \end{gathered} \tag{2.16}$$

where k_i is the exchange rate of protons in i going to pool j and vice versa for k_j.

The solution for Equation 2.16 can be expressed in the form

$$\mathbf{m}(t) = e^{-\mathbf{A}t}\mathbf{m}(0) \tag{2.17}$$

where $e^{\mathbf{A}t}$ is the matrix exponential and is defined by

$$\mathbf{Q}\mathbf{E}(t)\mathbf{Q}^{-1} = e^{\mathbf{A}t} \tag{2.18}$$

where $\mathbf{Q} = \mathbf{e}_1, ...\mathbf{e}_n$ is the eigenvectors with the corresponding eigenvalues $\lambda_1, ...\lambda_n$ and

$$\mathbf{E}(t) = \begin{bmatrix} e^{\lambda_1 t} & 0 & \cdots & 0 \\ 0 & e^{\lambda_2 t} & & \\ \vdots & & \ddots & \vdots \\ 0 & & \cdots & e^{\lambda_n t} \end{bmatrix} \tag{2.19}$$

are the solutions of the differential equation [19]. This solution holds for diagonalizable or non-diagonalizable matrices and the matrix exponential can be generally expanded using a power series as

$$e^{\mathbf{A}t} = \mathbf{I} + t\mathbf{A} + \frac{t^2\mathbf{A}^2}{2!} + \cdots. \tag{2.20}$$

A way to determine the matrix exponential involves using a polynomial method, where it can be expressed as [45]

$$e^{\mathbf{A}t} = \sum_{j=0}^{n-1} e^{\lambda_j t} \prod_{k=1, k\neq j}^{n} \frac{\mathbf{A} - \lambda_k \mathbf{I}}{\lambda_j - \lambda_k}. \tag{2.21}$$

In the two-pool model there are two eigenvalues and two eigenvectors, so Equation 2.21 becomes

$$e^{\mathbf{A}t} = e^{\lambda_1 t}\frac{\mathbf{A} - \lambda_2 \mathbf{I}}{\lambda_1 - \lambda_2} + e^{\lambda_2 t}\frac{\mathbf{A} - \lambda_1 \mathbf{I}}{\lambda_2 - \lambda_1} \tag{2.22}$$

and for our case of $-\mathbf{A}$ the matrix exponential can be written as

$$e^{-\mathbf{A}t} = g_0\mathbf{I} + g_1(t)\mathbf{A} \tag{2.23}$$

where

$$g_0(t) = \frac{\lambda_2 e^{-\lambda_1 t} - \lambda_1 e^{-\lambda_2 t}}{\lambda_2 - \lambda_1} \tag{2.24}$$

$$g_1(t) = \frac{e^{-\lambda_2 t} - e^{-\lambda_1 t}}{\lambda_2 - \lambda_1} \tag{2.25}$$

and λ_1 and λ_2 are the eigenvalues of the matrix $\mathbf{A}$ determined by

$$det[\mathbf{A} - \lambda \mathbf{I}] = 0. \tag{2.26}$$

Inserting Equation 2.24 and Equation 2.25 into Equation 2.23 and solving for the eigenvalues using Equation 2.26, the matrix exponential becomes

$$\begin{aligned} e^{-\mathbf{A}t} = \frac{1}{\lambda_2 - \lambda_1} \Bigg(\Big[\; \lambda_2 e^{-\lambda_1 t} - \lambda_1 e^{-\lambda_2 t} \; \Big] \\ + \begin{bmatrix} (k_i + \frac{1}{T_{2i}})(e^{-\lambda_2 t} - e^{-\lambda_1 t}) & -k_j(e^{-\lambda_2 t} - e^{-\lambda_1 t}) \\ -k_i(e^{-\lambda_2 t} - e^{-\lambda_1 t}) & (k_j + \frac{1}{T_{2j}})(e^{-\lambda_2 t} - e^{-\lambda_1 t}) \end{bmatrix} \Bigg) \end{aligned} \tag{2.27}$$

where λ_1 and λ_2 are given by

$$\lambda_{1,2} = \frac{(k_i + k_j + \frac{1}{T_{2i}} + \frac{1}{T_{2j}}) \pm [(-k_j + k_i + \frac{1}{T_{2i}} - \frac{1}{T_{2j}})^2 + 4k_i k_j]^{\frac{1}{2}}}{2}. \tag{2.28}$$

Thus the solution of the original differential given in Equation 2.16 is

$$\begin{aligned} \begin{bmatrix} m_i(t) \\ m_j(t) \end{bmatrix} = \frac{C_1}{\lambda_2 - \lambda_1} \begin{bmatrix} (\lambda_2 - k_i - \frac{1}{T_{2i}})e^{-\lambda_1 t} + (-\lambda_1 + k_i + \frac{1}{T_{2i}})e^{-\lambda_2 t} \\ -k_i(e^{-\lambda_2 t} - e^{-\lambda_1 t}) \end{bmatrix} \\ + \frac{C_2}{\lambda_2 - \lambda_1} \begin{bmatrix} -k_j(e^{-\lambda_2 t} - e^{-\lambda_1 t}) \\ (\lambda_2 - k_j - \frac{1}{T_{2j}})e^{-\lambda_1 t} + (-\lambda_1 + k_j + \frac{1}{T_{2j}})e^{-\lambda_2 t} \end{bmatrix} \end{aligned} \tag{2.29}$$

where $C_{1,2}$ are constants to be determined. Solving for $C_{1,2}$ using the initial conditions that $m_{i,j}(0) = P_{i,j}$, where $P_{i,j}$ is the probability that the spin is found in the state i or j and

$$P_i + P_j = 1 \tag{2.30}$$

then

$$C_1 = P_i$$

$$C_2 = P_j.$$

The final general solution of the ordinary differential equation becomes

$$M(t) = \alpha_i e^{-\lambda_1 t} + \alpha_j e^{-\lambda_2 t} \tag{2.31}$$

where

$$\begin{aligned} \alpha_i &= \tfrac{1}{\lambda_2 - \lambda_1}(\lambda_2 - \tfrac{P_i}{T_{2i}} - \tfrac{P_j}{T_{2j}}) \\ \alpha_j &= \tfrac{1}{\lambda_2 - \lambda_1}(-\lambda_1 + \tfrac{P_i}{T_{2i}} + \tfrac{P_j}{T_{2j}}). \end{aligned} \tag{2.32}$$

The eigenvalues of the equation, λ_i are the apparent relaxation rates and in the case of slow exchange (where $k_{i,j} \to 0$) the eigenvalues and their respective constants become

$$\begin{aligned} \lambda_1 &= \tfrac{1}{T_{2i}}, \qquad \alpha_i = P_i \\ \lambda_2 &= \tfrac{1}{T_{2j}}, \qquad \alpha_j = P_j \end{aligned} \tag{2.33}$$

and the magnetization equation reduces to

$$M(t) = P_i e^{-\frac{1}{T_{2i}}} + P_j e^{-\frac{1}{T_{2j}}} \tag{2.34}$$

where two separate decay times can be measured for two different water environments and the values measured experimentally are the correct, 'real' T_2 times of the environments.

Chapter 3

Evidence of 'Long-T_2' Times and Higher Myelin Content in the Corticospinal Tract

3.1 Introduction

In healthy white matter at least two water environments can be distinguished, one arising from MW and another from IE. In addition, a Long-T_2 component ($200ms < T_2 < 800ms$) has been observed in the white matter of subjects with phenylketonuria (PKU) and MS, as well in the posterior internal capsule (IC) of most normal subjects [34, 35]. A model T_2 distribution for structures with a Long-T_2 component can be seen in Figure 3.1, this is based on the results that Laule et al. [35] found for the posterior IC. The CST is contained within the posterior limb (PL) of the IC [24, 73] and is most likely responsible for the presence of Long-T_2 times observed in the IC [73]. The PLIC was also found to have a high myelin content than other white matter structures [70], the CST is expected to also have a high myelin content. The relationship between myelin content and the amount of Long-T_2 signal has not previously been studied in healthy white matter.

In this study, the relationship between the MWF and Long-T_2 fraction (LT_2F) was examined in the CST and the anterior internal capsule (AIC) using two different

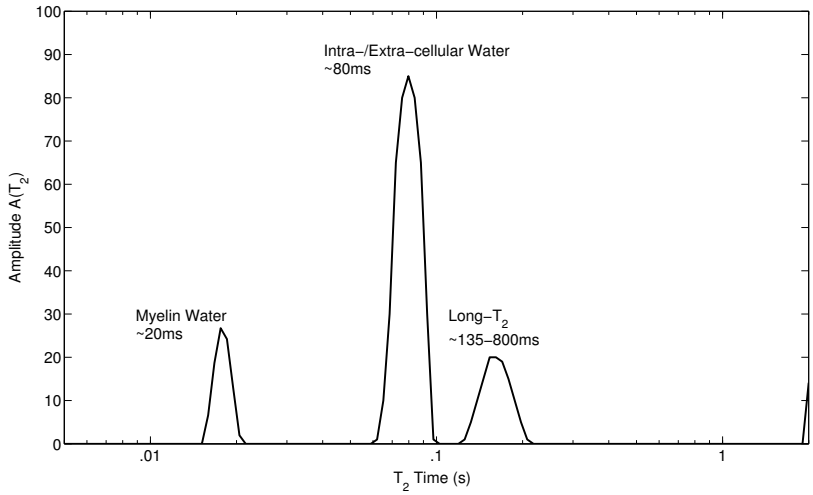

Figure 3.1: Expected T_2 distribution for a structure with a Long-T_2 component.

LT_2F T_2 ranges. The AIC was expected to have a low LT_2F based on LT_2F maps from an earlier study [35]. The T_2 distributions for the CST, the AIC and other white matter structures were also examined to look at the peaks in the area of the measured Long-T_2 signal.

3.2 Methods

3.2.1 Subject Information

Sixteen healthy subjects were selected for this study; one was rejected due to artifactually high MWF and another was rejected due to file corruption/motion artifacts. Fourteen normal healthy subjects were examined; mean age$= 26.6 \pm 4$ (SD) years (range$= 19 - 34$); 6 males and 8 females. The study was supported by a Vancouver Hospital and Health Sciences Centre Interdisciplinary Grant [58]. The research protocol was granted Ethical Approval by the UBC Clinical Research Ethics Board.

3.2.2 MR Studies

The research was carried out on a $1.5T$ MR scanner (Echo Speed; GE Medical Systems, Milwaukee, Wis) operating at version 5.7 of the software and hardware. After a localizer, proton density and T_2-weighted images ($TR/TE(ms)$, $2500/30$ and 80) were followed by a 48-echo modified CPMG sequence with variable repetition time [32, 58]. The T_2 sequences excited a single transverse slice ($5mm$ thick; 128×128 matrix, four averages) through the base of the genu and splenium of the corpus callosum. The echo spacing for the CPMG sequence was $10ms$ for the first 32 echoes and $50ms$ for the last 16 echoes [59]. To decrease the acquisition time, a variable repetition time (TR) was used; the TR was $3.8s$ for the 20 central lines of k-space and TR linearly decreased from $3.8s$ to $2.12s$ for the k-space extremities. The effect of this variable TR strategy on T_2 distributions is negligible [32].

3.2.3 Data Analysis

Regions of Interest (ROIS) were drawn on T_2-weighted images for the genu (the right or left side of the genu was used if the slice location made it not possible to take the entire genu and a Region of Interest (ROI) value for one subject was not obtainable) and splenium of the corpus callosum (CC) and bilaterally for the CST, AIC and major and minor forceps. Approximate locations of the ROIS can be seen in Figure 3.2. The location of the CST was taken as the bright focal area within the posterior IC on a heavily T_2-weighted image ($TE = 230ms$), Figure 3.2b [73]. T_2 analysis was completed using a program called AnalyzeNNLS [3]. This program carries out a regularized non-negative least squares fitting [37] of a multi-exponential decay curve [69]. The output T_2 distributions for each structure were compared.

The MWF was defined as the area under the MW peak divided by the total area under the T_2 distribution peaks for each ROI, the lower limit for MWF estimation was 5ms and the upper $40ms$. Changing the range of T_2 times over which the LT_2F is examined may have an effect on the relationship between LT_2F and MWF. To examine this, the LT_2F was defined in two different ways, using a variable Long-T_2 time range and a fixed Long-T_2 time range. The lower limit of the variable LT_2F was selected by observing LT_2F images with different T_2 time ranges, and choosing

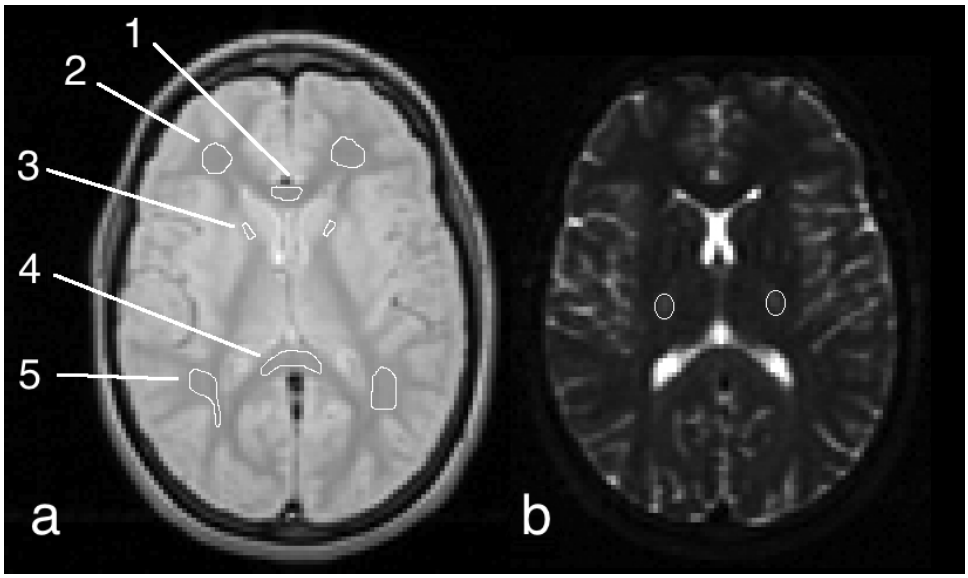

Figure 3.2: Axial image of one subject (a) T_2-weighted image $TE = 10ms$ with representations of the ROIS of different white matter structures 1) genu of CC, 2) minor forceps 3) AIC 4) splenium of CC and 5) major forceps. (b) Heavily T_2-weighted image TE=230ms with CST ROIS

the T_2 time range that gave rise to signal from the CST but not from the surrounding tissue for each subject separately, the lower limits ranged from $T_2 = 120-145ms$ (average $T_2 = 135ms$). In a second analysis, the aforementioned variable Long-T_2 range was changed to a fixed Long-T_2 range of $120-800ms$ for each subject. The variable LT_2F was determined by the fraction of signal arising from the Long-T_2 range, $(120-145)ms-800ms$ for the variable LT_2F, and $120-800ms$ for the fixed LT_2F, divided by the total signal from all T_2 times.

The MWF and LT_2F were determined for the CST and AIC. The average subject MWF and LT_2F for the CST and AIC were plotted against each other and examined using a linear regression for the two different LT_2F ranges. MWF and LT_2F maps were created for each subject by the fraction of each component within a voxel. Statistical analysis was completed using Student's t-test, a $p < 0.05$ was considered to be significant and the errors presented are standard errors.

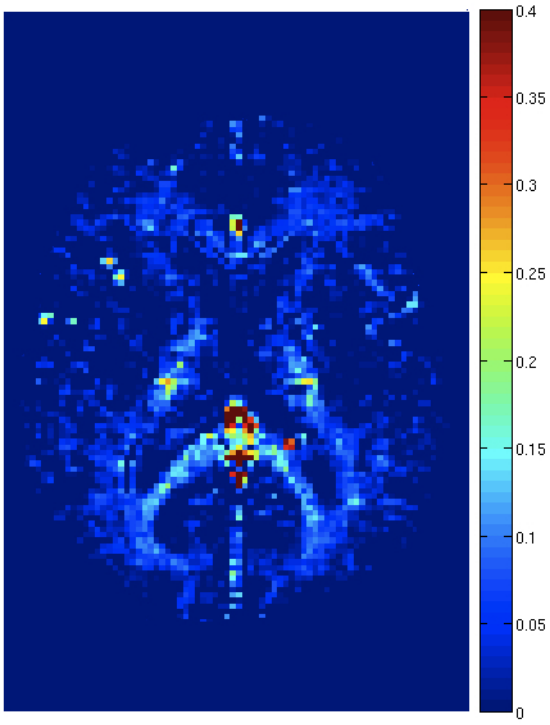

Figure 3.3: MWF map for one subject.

3.3 Results

The MWF map for one subject can be seen in Figure 3.3, the CST showed a higher MWF than the surrounding posterior IC and AIC. The average MWF for the AIC, $0.066(\pm 0.004)$, was 62.0% lower than the average MWF for the CST, $0.173(\pm 0.009)$, ($p < 10^{-10}$). The LT_2F map for one subject with the variable LT_2F range and fixed LT_2F range, are given in Figure 3.4 and Figure 3.5 respectively. The CST shows a distinct brighter intensity at longer T_2 times.

Using the variable range for LT_2F, the average LT_2F for the AIC, $1.9 \times 10^{-5}(\pm 1.9 \times 10^{-5})$ was 99.99% lower than the average LT_2F for the CST, $0.22(\pm 0.01)$, ($p < 10^{-16}$). The relationship between LT_2F using a variable LT_2F threshold for the CST and AIC can be seen in Figure 3.6. The LT_2F and MWF were moderately correlated in the CST, $R^2 = 0.4781$. This was not seen in the AIC as only one AIC ROI had a non-zero LT_2F.

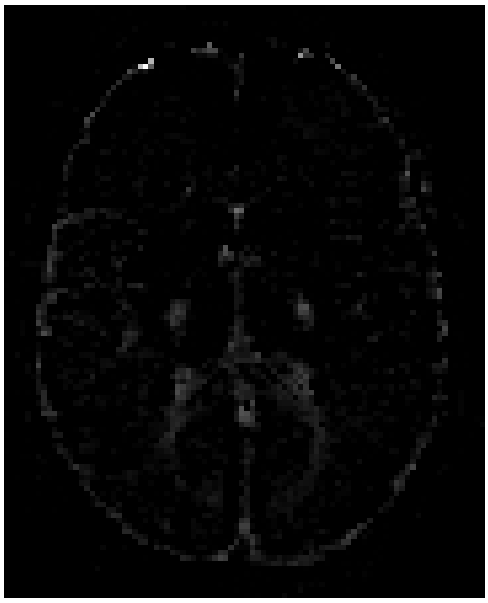

Figure 3.4: LT_2F map for one subject, $T_2 = 140ms - 800ms$

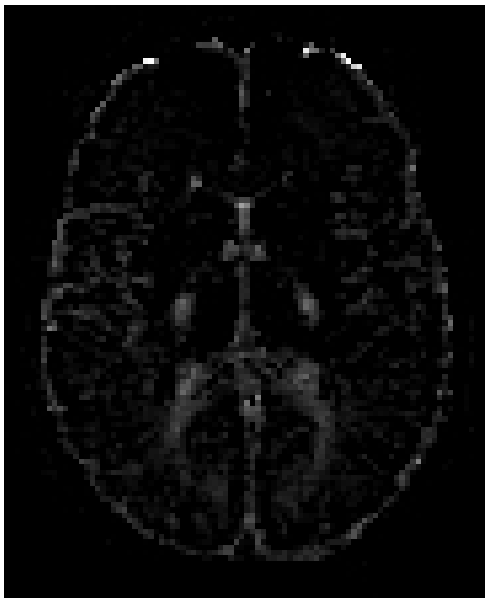

Figure 3.5: LT_2F map for one subject, $T_2 = 120ms - 800ms$

Using the fixed LT_2F range ($120ms - 800ms$), the average LT_2F for the AIC, $0.0011(\pm.0007)$, was 99.6% lower than the average LT_2F for the CST, which was $0.32(\pm.01)$. The relationship between LT_2F using a fixed threshold and MWF for the CST and AIC can be seen in Figure 3.7. The LT_2F and MWF are poorly correlated, $R^2 = 0.0231$, however the slope is still significant, $p < 10^{-6}$. This was not seen in the AIC as only two AIC ROIS had a non-zero LT_2F.

Changing the LT_2F threshold from a variable range to a fixed range appears to eliminate the relationship between LT_2F and MWF, the R^2 decreased from 0.4781 to 0.0231. The increase in LT_2F seen in Figure 3.6 may have been induced by changing the LT_2F threshold for each person, rather than from changes in MWF. The lower limits, which supposedly corresponding to the Long-T_2 peak, used for LT2F calculation had a significant impact on the relationship between MWF and LT_2F in the CST.

A sample of common T_2 distributions for different white matter structures are given for the variable LT_2F threshold, see Figure 3.8, and fixed LT_2F threshold, see Figure 3.9. The designated LT_2F T_2 range is highlighted in yellow on each T_2

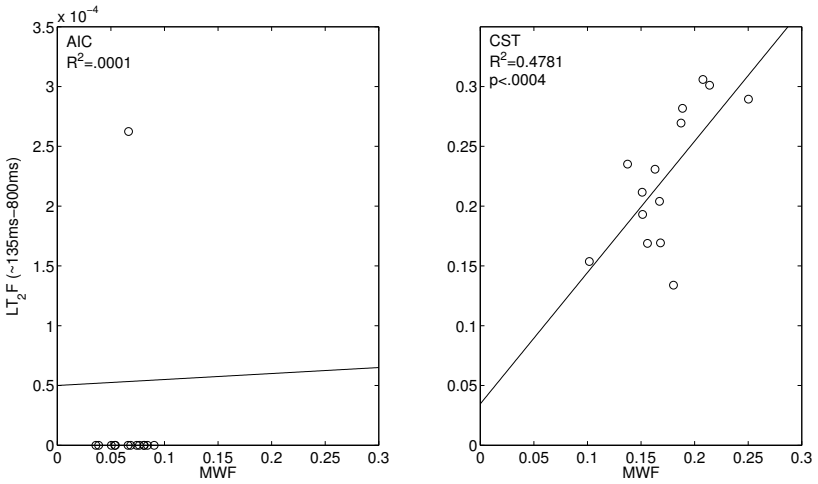

Figure 3.6: Relationship between variable range $\mathrm{LT_2F}$ ($T_2 = \sim 135ms - 800ms$) and MWF

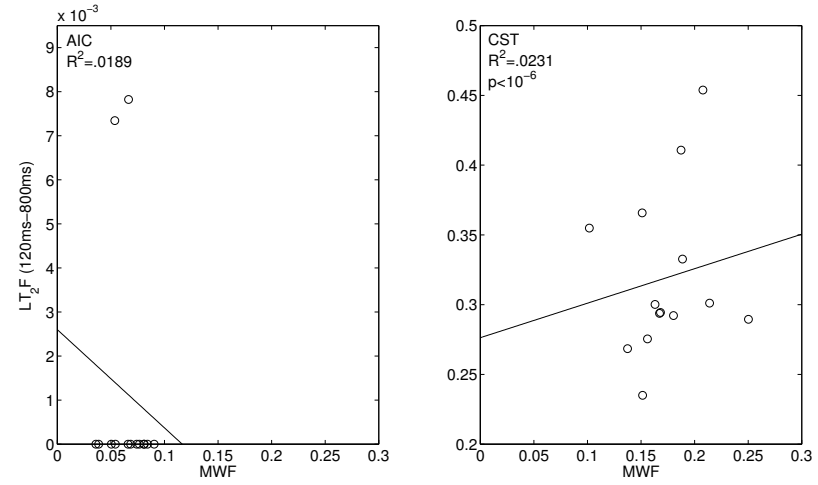

Figure 3.7: Relationship between fixed $\mathrm{LT_2F}$ ($T_2 = 120ms - 800ms$) and MWF

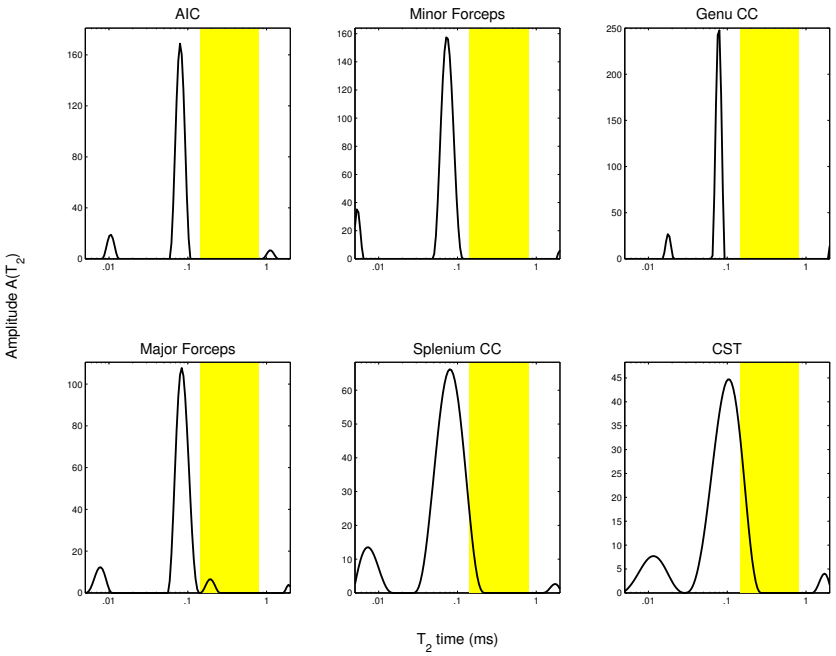

Figure 3.8: T_2 distributions for different white matter structures with highlighted variable LT_2F range ($T_2 = \sim 135ms - 800ms$)

distribution. It appears the LT_2F being measured is not from a separate Long-T_2 peak but rather from part of a broadened IE peak. CST ROIs also often show split peaks but this splitting usually occurs at lower T_2 times than $100ms$.

3.4 Discussion

The CST is different than other structures; it appears as a bright area on LT_2F images and MWF images, this was not seen in the nearby structure of the AIC or other white matter structures. This was reflected in the relationship between LT_2F using a variable LT_2F threshold and MWF seen in the CST. The relationship was not seen in the AIC. The T_2 distribution for a typical AIC ROI showed that no overlap between the LT_2F threshold and the IE peak. The strength of the relationship between LT_2F and MWF in the CST was diminished by changing the LT_2F threshold.

When the T_2 distribution of the CST was examined carefully it showed that the

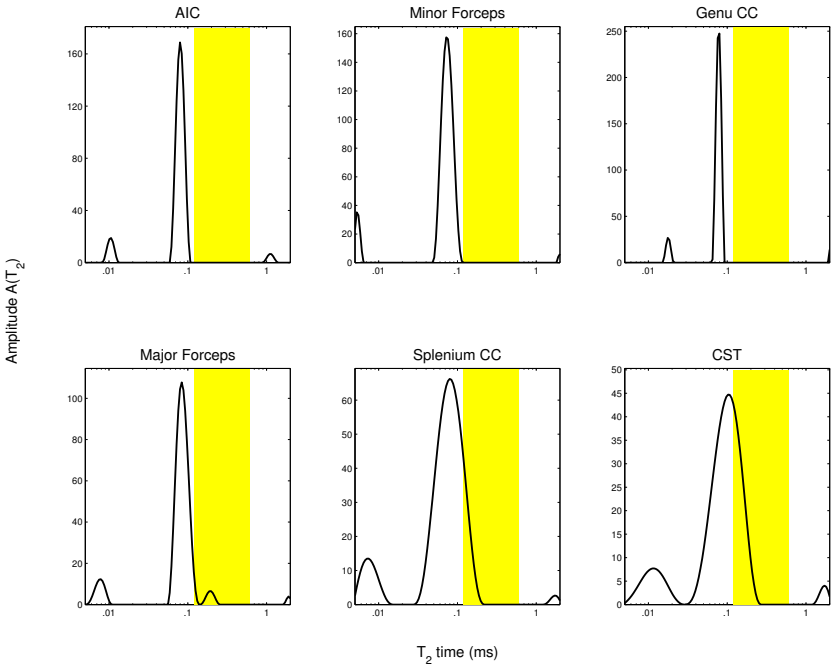

Figure 3.9: T_2 distributions for different white matter structures with highlighted fixed LT_2F range ($120-800ms$)

LT_2F was for the most part measuring part of the IE peak. The concept of Long-T_2 does not appear to be appropriate for the CST as changes in the measured LT_2F are the result of changes in the IE peak and is not arising from a separate water pool. The relationship between LT_2F and MWF seen in the CST does not appear to be real.

The higher MWF structures (the splenium of CC and CST) appear to have wider IE T_2 peaks centred at higher T_2. This was consistent with earlier results [70].

3.5 Conclusion

The relationship between LT_2F and MWF in the CST does not appear to be the result of a separate T_2 peak at higher T_2 times (i.e. another water environment), but rather the result of the IE peak characteristics. The LT_2F is not an appropriate measure for comparing between healthy white matter structures, though it has been used

successfully to compare healthy tissue to pathological tissue [35]. The possible relationship between MWF and the T_2 peak location will be examined in Chapter 5.

Chapter 4

Origin of the Bright Signal in the Corticospinal Tract on T_2-weighted Images and Myelin Water Images.

4.1 Introduction

For most normal healthy adult subjects, the CST can be identified on heavily T_2-weighted MR images as a bright focal region, and on T_1-weighted images as a darker area [73]. Bright regions in the CST, which are thought to be qualitatively different than healthy bright regions [73], sometimes occur in the motor neuron disease amyotrophic lateral sclerosis (ALS) and were previously thought to be a sign of pathology [14, 18]. However, these areas have been found to be insignificantly different from the CST of healthy tissue for T_2 measurements made using two TEs [23] and using a 32 echo pulse sequence with a monoexponential fit [27]. Since bright regions on T_2-weighted images can also be an indicator of pathology, properly characterizing and identifying what gives rise to the bright areas of the CST in healthy normal tissue is important.

The CST is an important descending nerve fibre tract that originates in the cere-

bral cortex, travels through the PL of the IC [24, 73] and finally into the spinal cord [47, 50]. The CST is responsible for distinct, voluntary motor movements [50] and has over 1 million fibres in each tract; the majority of these fibres are small in size (90%) but 3.5% of the fibres are very large axons ($>20\mu$m) up to 22μm [28, 29, 50]. At the level of the IC the fibre morphology of the CST was found to be mostly large diameter axons (implying large myelin sheaths [55]) of low density when compared to areas directly anterior and posterior [73]. These morphological properties of the CST presumably give rise to its unique appearance on MR images.

A variety of MRI methods including diffusion tensor imaging (DTI), magnetization transfer ratio (MTR), and T_2 relaxation have been used to characterize the CST in brain [22, 53]. T_2 relaxation is influenced by the interactions of water protons with protons on other molecules (non-aqueous) in its vicinity and is also affected by water diffusion on the timescale of the experiment [40, 70]. In healthy white matter, T_2 decay curves are multiexponential and can be separated into at least two components, which arise from different water environments [38, 43, 70]. The shortest component ($\sim 20ms$) is from MW, which is water trapped between the myelin sheaths in white matter; a longer T_2 ($\sim 80ms$) arises from IE (intracellular is also called intra-axonal) [38, 42, 44, 62]. The MWF is defined as the fraction of the T_2 distribution in the shorter T_2 component. MWF was found to correlate with myelin content in histological studies [15, 16, 31, 36, 46, 67]. The shape of T_2 distributions from different structures can provide biological information as well as be used to compare healthy and pathological tissue [34, 35, 58].

The PLIC containing the CST has unique MR relaxation properties, which is unsurprising given its appearance on MR images. Yagishita et al. [73] proposed the CST had longer T_2 and T_1 times in the IC, when compared to areas directly anterior and posterior. In a more recent study with a monoexponential T_2 analysis, the CST itself was reported to have, on average, longer T_2 and T_1 times, as well as lower MTR values when compared to regions directly anterior [22]. In another study, which used 48 TE times and calculated T_2 distributions, the PLIC showed evidence of a water reservoir with longer T_2 times (signal arising in the range of $T_2 = 200m - 800ms$) in $10/15$ healthy subjects; this was not seen in any other healthy white matter structures examined but was found in pathological white matter in phenylketonuria and multiple sclerosis lesions [35]. In a study of normal

healthy brain structures Whittall et al. [70] found that compared to other cerebral white matter structures, the PLIC had a higher MWF than surrounding tissue and thus appeared bright on MWF maps. As well, Whittall et al. [70] found that the PLIC had the highest T_2 for the IE peak compared to all other white matter structures examined and the highest IE peak distribution width of all structures; the widening of the IE peak could be a reflection of morphological inhomogeneities [62, 70]. Furthermore, the IE peak in the CST and the splenium of CC were found to often split into two peaks while other white matter structures rarely exhibited this behaviour Whittall et al. [70]. T_2 measurements with limited TE coverage [22] are known to produce inaccurate results [71] and multi-echo sequences for which the longest TE time is $320ms$ [70] are sub-optimal for accurate detection of the longer T_2 times of IE peak in the CST [59].

The goal of this study was to re-examine the T_2 behaviour of the CST using a pulse sequence especially designed to provide more accurate T_2 distributions for the IE T_2 peak [59]. Our T_2 sequence made use of 48 echoes, extending to a final echo at $1120ms$. Our study focused on the characteristics and shape of the T_2 distributions of various white matter structures in the vicinity of the CST with the aim to understand, in terms of the T_2 distribution, why the CST appears bright on heavily T_2-weighted images and MWF maps in comparison to other structures. In addition, areas posterior and anterior to the CST were examined to compare with results from earlier literature.

4.2 Methods

4.2.1 Subject Information

See Section 3.2.1.

4.2.2 Magnetic Resonance Studies

See Section 3.2.2.

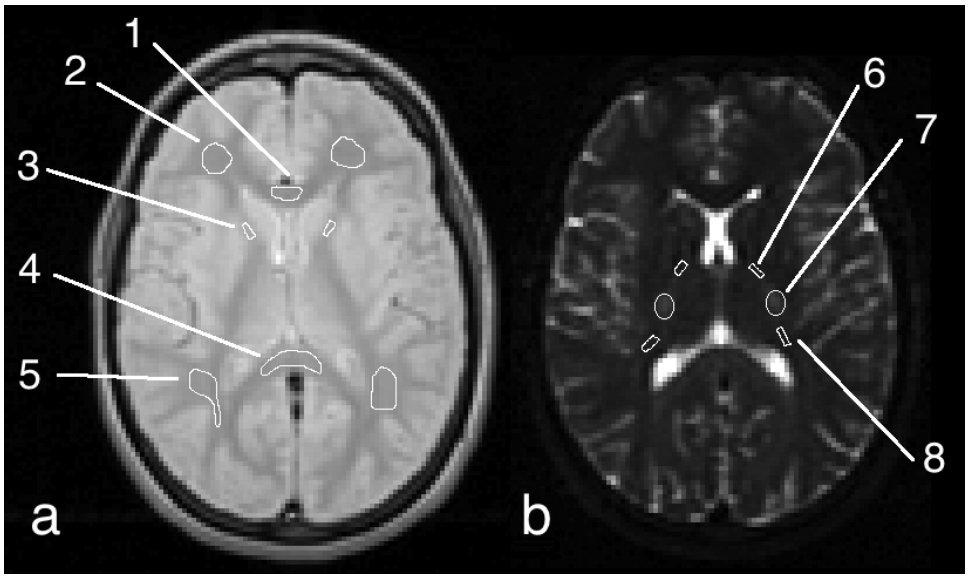

Figure 4.1: Axial image of one subject (a) T_2-weighted image $TE = 30ms$ with representations of the ROIs of different white matter structures 1) genu of CC, 2) minor forceps 3) AIC 4) splenium of CC and 5) major forceps. (b) Heavily T_2-weighted image TE=230ms 6) Anterior to CST 7) CST 8) Posterior to CST.

4.2.3 Data Analysis

ROIS were drawn on T_2-weighted images as outlined in Section 3.2.3, but the CST was redrawn to be more conservative to only include the brightest area on the heavily-weighted T_2 images ($TE = 230ms$). As well, the previously unobtainable genu ROI was included. Approximate locations of the ROIS can be seen in Figure 4.1a. As well, areas anterior and posterior to the CST were drawn bilaterally sufficiently separated that they would not overlap with CST, which spreads out as the tract leaves the spine and travels upwards into higher slices [50]. These anterior and posterior ROIS were taken outside the bright area on the $TE = 230ms$ echo and drawn on the 1st echo to avoid overlap with other structures. An example of the anterior and posterior to CST ROIS can be seen in Figure 4.1b. T_2 analysis was completed using a program called AnalyzeNNLS [3]. This program carries out a regularized nonnegative least squares fitting [37] of a multi-exponential decay

curve [69]. The output T_2 distributions for each ROI were then summed together for each structure and normalized by dividing the distribution by the maximum summed signal intensity, allowing for examination and comparison between structures of the general T_2 distribution shape. The MWF was defined as the area under the MW peak divided by the total area under the T_2 distribution peaks for each ROI; the lower limit for MWF estimation was 5ms and two MWF upper limits were used, $40ms$ and $25ms$. The position of the IE peak was examined using the geometric mean T_2 (GMT_2), which is the mean T_2 on a logarithmic scale. Given by

$$gmT_2 = exp\left[\frac{\sum_{T_{2min}}^{T_{2max}} S(T_2)\log T_2}{\sum_{T_{2min}}^{T_{2max}} S(T_2)}\right] \tag{4.1}$$

for a given peak defined from T_{2min} to T_{2max} [3, 69] where T_{2min} was the designated boundary between MW and IE water ($25ms$ or $40ms$) and $T_{2max} = 600ms$. The limit of 600ms was chosen to avoid overlap with cerebrospinal fluid (CSF), but to include IE signal from the CST in the $400-600ms$ range, no other structure had signal in this range. All errors are reported as standard deviations unless otherwise stated. Student's t-test was used to test significant differences between MWFs of the CST and three other ROIs (splenium of CC, anterior to CST and posterior to CST). Bilateral structures right and left were examined separately. The p values were Bonferroni corrected, there were 21 t-tests, so $p < 0.0024$, was considered to be significant. Significance was also tested between the two MW/IE interface limits $25ms$ and $40ms$ for each structure and Bonferroni corrected, $p < 0.003$ was considered to be significant.

4.3 Results

The summed and normalized T_2 distributions for each structure can be seen in Figure 4.2. Figure 4.2a demonstrates that the CST T_2 distribution had a distinctly different shape from other white matter structures and in particular from anterior and posterior white matter areas, see Figure 4.2b. The CST IE peak was both shifted to higher T_2 times and distributed over a wider range of T_2 times. The CST had an atypical T_2 distribution shape; the IE peak was split into two subsidiary peaks in

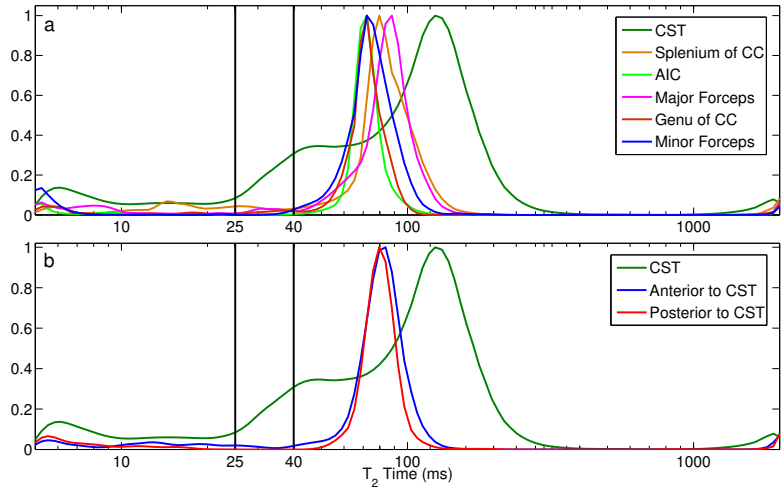

Figure 4.2: Normalized summation of T_2 distributions with vertical lines drawn at 25ms and 40ms to show MWF/GMT$_2$ limits comparing a) CST and other white matter structures and b) CST and areas anterior and posterior to CST

50% of the ROIs. The summed and normalized T_2 distribution of the CST split or no-split distributions can be seen in Figure 4.4 compared to one of the "normal" T_2 distributions, that of the splenium of the CC. In summary, the NNLS T_2 distributions from the CST imply that the CST possesses two separate water reservoirs, one with T_2 of approximately 40ms and the other with T_2 of approximately $120ms$. Depending upon the signal to noise of the T_2 decay curve in the NNLS analysis, these two peaks may appear as two separated peaks or as a single broad T_2 peak.

The MWF map $(5-40ms)$ for one subject can be seen in Figure 4.3a, the CST appears bright compared to other white matter areas, meaning higher MWF. However, based on Figure 4.2 and Figure 4.4 it appears that part of the IE peak overlaps with the region designated for MW and the MWF is consequently artificially increased. A MWF map for $5-25ms$ can be seen in Figure 4.3b. There was a general but slight decrease in MWF for most white matter structures, but contrast between the CST and other structures was no longer evident. The average MWF and percent change between the two upper limits were determined for all structures and is given in Table 4.1. The average MWF for the CST went from $0.19(.05)$ to $0.11(.04)$ and

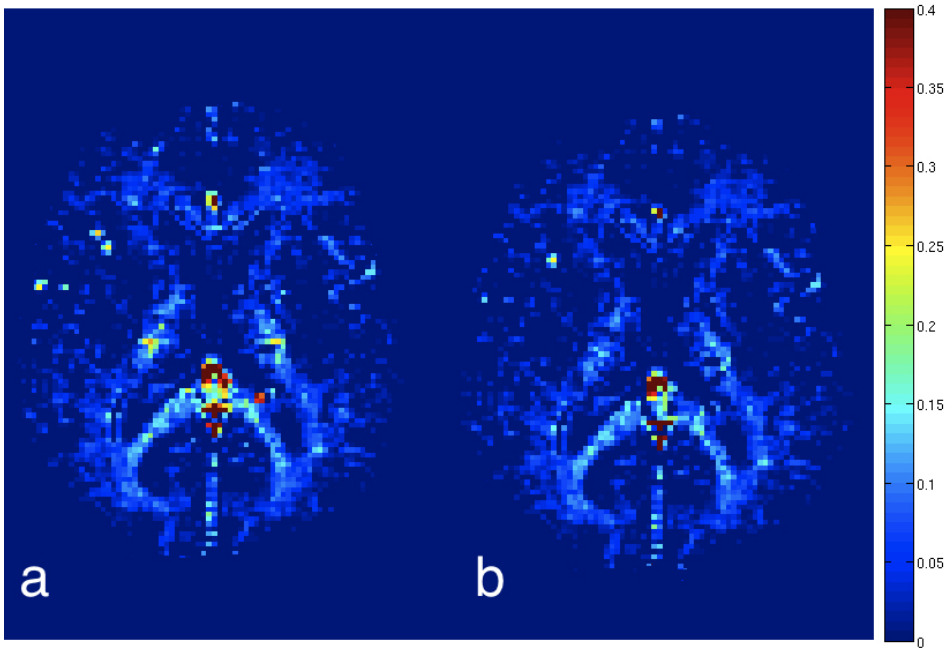

Figure 4.3: MWF maps for one subject with two different T_2 ranges; a) $5-40ms$ and b) $5-25ms$.

Table 4.1: Changes in MWF for two different cutoffs in white matter structures.

Structure	MWF (5-40ms)	MWF (5-25ms)	% MWF Change	p-value
CST	0.19(.05)	0.11(.04)	8.5	$\mathbf{2.11 \times 10^{-6}}$
Splenium of CC	0.14(.04)	0.11(.04)	3.5	0.061
Major Forceps	0.11(.04)	0.086(.02)	2.5	**0.0021**
Anterior to CST	0.11(.03)	0.095(.03)	1.7	0.010
Posterior to CST	0.098(.02)	0.096(.02)	0.1	0.32
Genu of CC	0.085(.03)	0.060(.03)	2.5	0.041
Minor Forceps	0.074(.02)	0.069(.02)	0.6	0.040
AIC	0.066(.02)	0.060(.03)	0.6	0.12

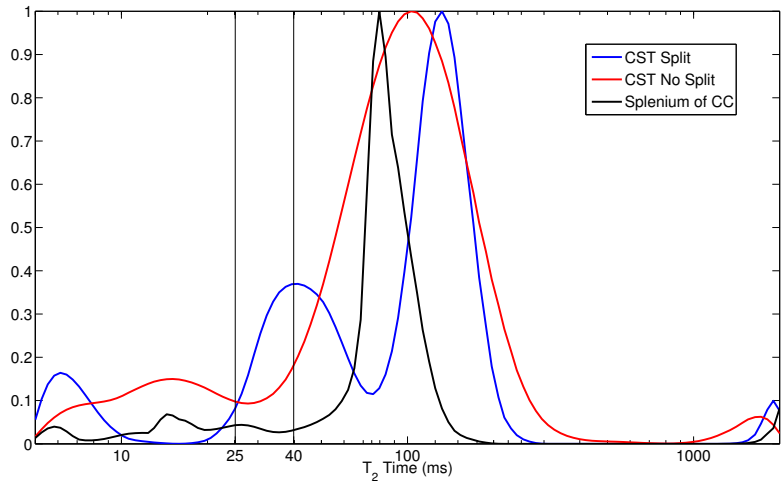

Figure 4.4: Normalized summation of T_2 distribution of CST where it splits and doesn't split into two peaks compared to the splenium of the CC with vertical lines drawn at 25ms and 40ms to show MWF/GMT$_2$ limits

was similar to the mean MWF found for the splenium of the CC, which was initially at $0.14(.04)$ and decreased to $0.11(.04)$ when the cutoff was changed. For the $25ms$ limit, the MWF of the splenium was not significantly different from the MWF from the CST ($p > 0.5$). With the $40ms$ cutoff, the areas anterior and posterior to the CST had a MWF of $0.11(.03)$ and $0.098(.03)$ respectively and all right and left ROIs were significantly different than the CST ROIs ($p < 0.002$). By moving the cutoff to $25ms$, the anterior and posterior region MWFs decreased to $0.095(.03)$ and $0.096(.03)$ respectively, and they were no longer significantly different from the CST ($p > 0.07$). It therefore appears that the two peaks from the CST contributed non-negligible signal intensity in the T_2 range of $25-40ms$ thereby artificially increasing the estimated MWF. Changes in the IE T_2 peak location were examined by changing the IE GMT$_2$ range from $40-600ms$ to $25-600ms$. The results for all structures examined can be seen in Table 2. The CST had the largest changes in IE GMT$_2$ and MWF. The CST T_2 distribution clearly differed from that of other structures, which show much less signal in the $25-40ms$ range and thus very little change in IE GMT$_2$ when the lower limit was reduced to $25ms$. The CST and the

Table 4.2: Changes in IE GMT_2 for two different cutoffs in white matter structures.

Structure	IE GMT_2 (40-600ms)	IE GMT_2 (25-600ms)	% Change	p-value
CST	104.8(8)	93.6(6)	10.7	$\mathbf{5.4 \times 10^{-6}}$
Splenium of CC	85.5(8)	81.8(6)	4.3	0.063
Major Forceps	84.2(4)	82.0(3)	2.7	**0.0028**
Anterior to CST	81.4(4)	79.9(3)	1.9	0.015
Posterior to CST	80.0(3)	80.0(3)	0.1	0.47
Minor Forceps	74.6(3)	74.3(2)	0.4	0.042
AIC	72.4(4)	72.0(3)	0.6	0.14
Genu of CC	72.2(3)	70.7(3)	2.0	0.029

major forceps were the only structures that were significantly different for the two different limits, $p < 10^{-5}$ and $p < 0.003$ respectively, for both MWF and IE GMT_2.

4.4 Discussion

T_2 distribution characteristics can provide information about different water environments in brain. Decreased proximity to non-aqueous protons, such as those on phospholipid head groups, cause less dephasing of the transverse magnetization, hence the T_2 times increase [40]. Laule et al. [35] previously reported bright areas on some long-T_2 maps (fraction of T_2 signal from $200ms - 800ms$) in the area of the IC of normal subjects, showing an increased amount of the longer T_2 component in this structure. Here we characterized the T_2 distribution of the CST using a 48-echo sequence extending to $1.120s$ and found the IE GMT_2 shifted to higher T_2 times causing the CST to appear bright on T_2-weighted images, in agreement with the previous literature [22, 53, 73].

The CST was also found previously to have increased MWF compared to surrounding tissue [70] contradicting the earlier histology studies from Yagishita et al. [73] who reported a lower density of axons and thus proposed that the CST had lower myelin density compared to surrounding areas. Figure 4.2, Table 4.1, and Table 4.2 demonstrate that a non-negligible amount of signal in the CST arose from water with T_2 times in the range of $25 - 40ms$. This suggests that it was not in-

creased myelin density that caused the bright focal regions of the CST on MWF images, but rather the extension of the CST IE peak into the MW T_2 region. The frequent appearance of split peaks in the CST most likely reflects the presence of two distinguishable water environments. The most likely candidates for these two environments are intra-axonal water and extracellular water. Two possible explanations for this anomalous behaviour of the CST IE T_2 peak are increased extracellular water or decreased exchange. We believe that the most likely explanation for the unique shape of the CST T_2 distribution is increased CST extracellular water in comparison to the other structures [22, 70, 73]. From histology the CST is known to have larger extracellular spaces compared to areas directly adjacent [73]. In Figure 2b the areas anterior and posterior to the CST exhibited much narrower IE peaks at lower GMT_2 times when compared to the CST. When there is large extracellular water spaces, water protons in these extracellular spaces will have limited interactions with nonaqueous protons, such as membrane surfaces, and should have longer T_2 times. These unique CST T_2 distribution characteristics appear to also be responsible for its appearance on MWF maps; separation of the peaks could push the intracellular water to lower T_2s thereby causing the intracellular water peak to overlap with the MW peak. Alternatively, the separation of the two water environments in the CST could arise from a decrease in exchange between intraaxonal and extracellular water due to the presence of thicker myelin sheaths in the CST compared to adjacent white matter [9, 21, 35, 70]. Other structures having smaller axons compared to the CST, such as the splenium and genu of the CC, which have axons up to $4-5\mu m$ and $3-4\mu m$ respectively [1], may experience greater exchange between the intracellular and extracellular water pools [9, 21]. Yagishita et al. [73] found smaller closely packed axons in the regions anterior and posterior to the CST. Increased exchange should cause not only a decreased GMT_2 time but also a narrowing of the IE peak [4, 74]. This could explain why the consistent splitting of the IE peak seen in the CST is not as often seen in other structures. Whether water exchange between the intracellular and extracellular regions occurs on the timescale of the T_2 experiment, and therefore would have a large influence on the T_2 measurements, is still in question. Two bovine studies found that exchange was too slow to affect the measurements dramatically on the timescale of T_2 experiments [4, 61] and a recent in vivo human brain study found that exchange

had little effect on MWFs in several brain structures [25]. Other studies in rat spine determined that exchange did affect the T_2 values appreciably [9, 21].

4.5 Conclusions

By using a T_2 relaxation measurement designed to better explore the shape of the T_2 distribution at times in the vicinity of 100ms, this study found the corticospinal tract gave rise to a summed T_2 distribution with a IE peak which was not only shifted to longer times but also exhibited a second IE peak with a shorter T_2 time. The shift of the IE peak to longer T_2 times is responsible for the bright focal regions observed on heavily T_2-weighted images of the CST. The additional IE component with shorter T_2 times caused bright regions of MWF maps due to overlap of the IE peak into the myelin water window. It is postulated that the mechanism for this shift and broadening of the IE peak is due to the presence of significantly more extracellular water in the corticospinal tract. Magnetization exchange on the timescale of the experiment may also play a role in creating the CST's anomalous T_2 distribution. The cortical spinal tract is a unique structure that has unique MR characteristics; hence special considerations are required when interpreting MR results from it.

Chapter 5

Increased Myelin Content Correlates with the Longer T_2 Times of the Intra-/Extra-cellular Water in White Matter Structures

5.1 Introduction

Whittall et al. [70] found the ranking of white matter structures from highest to lowest MWF, and highest to lowest IE GMT_2, were the same (highest to lowest: PLIC, splenium of CC, major forceps, genu of CC and minor forceps). Although this ranking was not exactly the same as was found in Chapter 4 using the $5-25ms$ T_2 time range for MWF (see Table 4.1 and Table 4.2), the CST still had the highest MWF (tied with the splenium of CC) and highest IE GMT_2 of all structures examined. In the current study the relationship between MWF and IE GMT_2 was examined in more detail with the goal of finding an explanation for this result.

In Chapter 4, it was found that high measured MWF in the CST could be the result of a widened IE T_2 peak extending into the MW peak area. These results sug-

gested that a more conservative T_2 time range of $5-25ms$ would be more appropriate for the CST, rather than the conventional $5-40ms$ range. The conventional T_2 range was found to be appropriate for other structures; there were no significant changes in MWF between the two T_2 ranges for the non-CST structures, with the exception of the major forceps (see Table 4.1).

It was found that the CST IE peak not only extended to lower T_2 times but also to higher T_2 times, which was most likely due to increased extracellular water with longer T_2 times. To accommodate the broadening of the CST IE peak, for the IE GMT_2 a $T_{2max} = 600ms$ was used to encompass the entire IE peak and the IE GMT_2 from $25-600ms$ was compared to $40-600ms$. Again, it was found that there were no significant changes in IE GMT_2 between the two T_2 ranges for the non-CST structures, with the exception of the major forceps (Table 4.2). Based on the results from Chapter 4, the MW/IE T_2 time interface was taken to be $25ms$ for this current study.

5.2 Methods

5.2.1 Subject Information

See Section 3.2.1.

5.2.2 MR Studies

See Section 3.2.2.

5.2.3 Regularization

In NNLS fitting of multi-exponential T_2 data the convention is to present T_2 distributions as rounded peaks. This is based on the fact that regularized T_2 distributions are more robust in the presence of noise and the assumption that real tissue data has broad peaks [69]. As shown in Equation 2.14, a regularization factor, μ, is added to modify the shape of the peaks. Common practice for analysis of T_2 data involves minimizing Equation 2.14 using the constraints given in Equation 2.15; this gives rise to widened curved peaks, see Figure 5.1. In the case of no regularization, $\mu = 0$, the peaks present as discrete spikes, which can be seen in Figure 5.1. Reg-

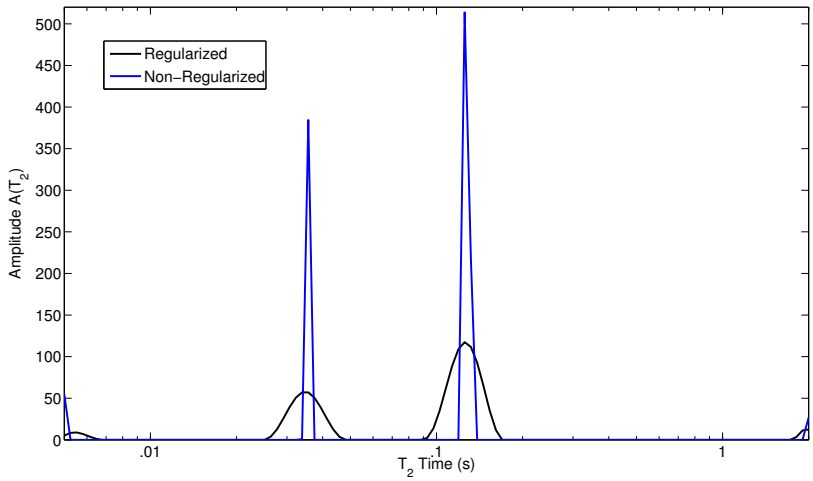

Figure 5.1: Regularized and non-regularized T_2 distribution for one CST ROI.

ularization can have an effect on the position of the T_2 peak, especially when two water environments are combined into one peak, which often occurs in IE. To examine what effect the regularization may have on the relationship between IE GMT_2 and MWF, these two quantities were collected with and without regularization.

5.2.4 T_2 Simulation

A series of simulations were performed to examine the effects of the NNLS fitting algorithm on IE GMT_2 in the presence of increasing MWF. Artificial multi-component decay curves were computed given a T_2 distribution with two discrete peaks corresponding to MW ($T_{2MW} = 0.020s$) and IE water ($T_{2IE} = 0.065s$). T_{2IE} was chosen based on the lowest IE GMT_2 found experimentally, which was in the AIC, $T_{2IE} = 65.8ms$. The input intra-/extra-cellular water fraction (IEF) was determined by

$$IEF = 1 - MWF. \tag{5.1}$$

For 49 MWF values linearly spaced between 0.02 and 0.5, 100 realizations of Rician noise (Gaussian on two channels) were added according to a prescribed signal-to-noise-ratio (SNR) of 100. The noisy decay curves were analyzed using the regular-

Table 5.1: Initial "no exchange" input parameters for a two-pool model

$T_{2MW}(ms)$	P_{MW}	$T_{2IE}(ms)$	P_{IE}
20	0.200967	100	0.799033

ized NNLS technique to create a T_2 distribution (see Section 2.3), from which the output GMT_2 and output MWF were extracted. In this way, for each inputted value of MWF, the mean calculated GMT_2 was determined and the output MWF and GMT_2 were compared.

5.2.5 Exchange Model

The general magnetization equation for two-pool exchange model, Equation 2.31, was used to model our system [10, 74]. The two water pools were assumed to be $i = MW$ and $j = IE$. An initial no-exchange starting point was used, where it was assumed $k_{MW,IE} \to 0$ causing Equation 2.31 to reduce to Equation 2.34. The introduction of exchange between MW and IE was modelled by increasing k_{MW}, k_{IE} was calculated from the input k_{MW} using [4, 17]

$$k_{IE} = \frac{P_{MW}}{P_{IE}} k_{MW}. \tag{5.2}$$

where $P_{MW} = MWF$ and $P_{IE} = IEF$ (see Equation 5.1), at the no-exchange limit. The resultant output probabilities and decay times were determined using Equation 2.28 and Equation 2.32 respectively.

The initial "no-exchange" values that were input into the exchange model are given in Table 5.1. The initial P_{MW} was taken from the largest experimental MWF of all the ROIS and the input T_{2IE} was its associated GMT_2. The output apparent IE GMT_2 (λ_2) was plotted against apparent MWF (α_{MW}) and compared to the experimental IE GMT_2 and MWF to determine whether exchange could account for their relationship found experimentally.

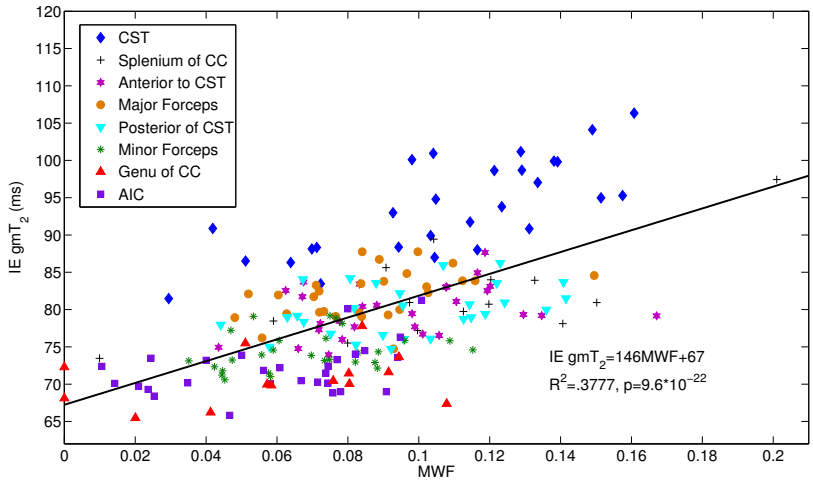

Figure 5.2: Relationship between IE GMT_2 and MWF across all structures and all subjects

5.2.6 Data Analysis

See Section 3.2.3. The ROIS from Chapter 4 were used and MWF was calculated using the new T_2 time range of $5-25ms$. The relationship between IE GMT_2 and MWF was examined by a linear regression for all structures together and each structure individually. The errors reported in the measurements are the standard errors. A Students t-test was used to determine whether the slope for all structures and each individual structure was significant. The p-values for the comparison of IE GMT_2 and MWF in individual structures were Bonferroni corrected so a $p < 0.00625$ was considered to be significant, otherwise $p < 0.05$ was considered to be significant.

5.3 Results

The relationship between IE GMT_2 and MWF has been presented in three different ways. First, all structures (all ROIs) for all 14 subject were examined, see Figure 5.2. The IE GMT_2 and MWF showed a moderate correlation of $R^2 = 0.3771$ and a significant linear slope ($p = 9.61 \times 10^{-22}$) (see All Structures in Table 5.2). Second, each structure was examined individually across the 14 subjects, the re-

Table 5.2: Results of linear regression analysis between IE GMT_2 and MWF

Structure	Slope	R^2	p-value
All Structures	146 ± 13	0.3777	$\mathbf{9.61 \times 10^{-22}}$
Average	313 ± 77	0.7319	$\mathbf{6.75 \times 10^{-3}}$
CST	136 ± 77	0.5555	$\mathbf{5.35 \times 10^{-6}}$
Splenium of CC	96 ± 29	0.4835	**0.0058**
Major Forceps	65 ± 26	0.1966	0.018
Anterior to CST	42 ± 23	0.1122	0.081
Posterior to CST	47 ± 23	0.1401	0.050
Genu of CC	29 ± 28	0.0870	0.31
Minor Forceps	33 ± 23	0.0772	0.15
AIC	54 ± 22	0.1822	0.024

sults from the linear regression analysis for IE GMT_2 verses MWF for each structure are given in Table 5.2. It appears that the same relationship between IE GMT_2 and MWF does not hold in every individual structure. The CST and splenium of CC had the highest slopes of all structures and are the only structures that showed a significant individual relationship between IE GMT_2 and MWF. Third, the relationship between average IE GMT_2 and average MWF across all subjects for each structure was examined, see Figure 5.3. A strong correlation between average IE GMT_2 and average MWF was found, $R^2 = 0.7319$ (see Average in Table 5.2).

The effect of $\mu = 0$ on the relationship between IE GMT_2 and MWF was examined by plotting these two values for the non-regularized and the usual regularized situation, shown in Figure 5.4. The introduction of regularization did not have a large effect on the slope of the linear regression or the correlation between IE GMT_2 and MWF. Regularization appears to bring in outliers at the higher MWF values and appears to push the peaks further in the MWF range.

The output IE GMT_2 and MWF from the NNLS simulations were plotted, Figure 5.5. Increasing the amplitude of the MW peak (increasing MWF) by a factor of 10 resulted in a decrease in IE GMT_2 of about $2ms$, while in the experimental data the same change in MWF resulted in an increase of IE GMT_2 from $65ms$ to $\sim 100ms$. Therefore, fitting with NNLS is not likely to be responsible for the relationship between IE GMT_2 and MWF across all structures.

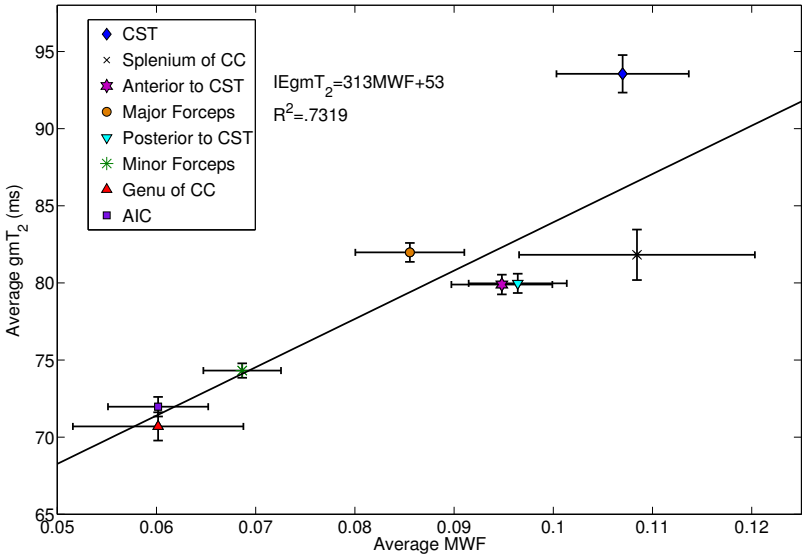

Figure 5.3: The average IE GMT_2 and MWF for white matter structures across subjects

The output apparent IE GMT_2 and MWF in the presence of exchange with the initial parameters from Table 5.1 are plotted in Figure 5.6a. The exchange model had a higher slope than the slopes found in the experimental data for individual structures and across all subjects and structures. Thus, the exchange model was compared with the regression for the averages of each structure, which had the highest slope. Exchange does not appear to give rise to the same relationship between IE GMT_2 and MWF that was found in the experimental data. The initial input parameters were modified in an attempt to fit the exchange model to the experimental data. Using the parameters listed in Table 5.3 the experimental data could be well modelled using exchange, see Figure 5.6b.

5.4 Discussion

Examining relationships between different quantitative brain measures may provide additional information about the underlying anatomy. The significant rela-

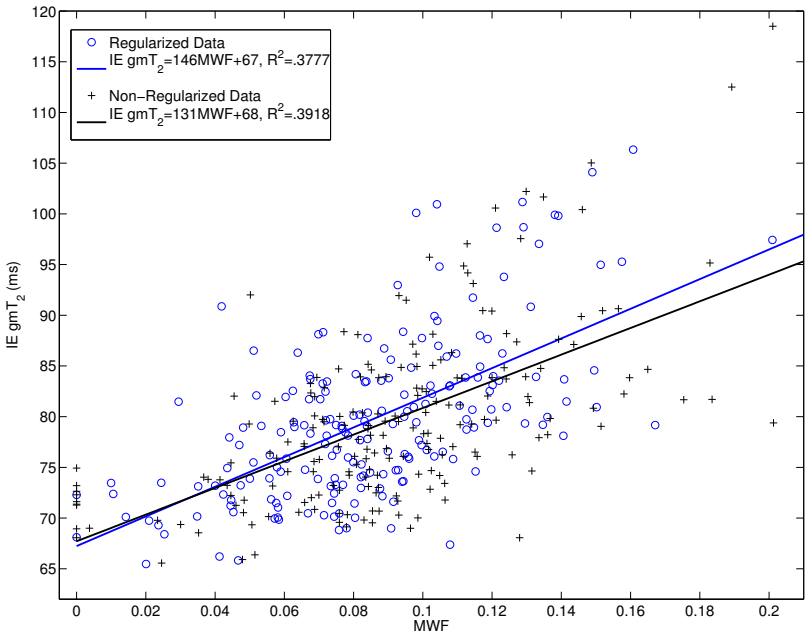

Figure 5.4: Relationship between IE GMT_2 and MWF across all structures for regularized and non-regularized NNLS fitting.

Table 5.3: Initial "no exchange" input parameters for a two-pool model that were found to fit the experimental model best

$T_{2MW}(ms)$	P_{MW}	$T_{2IE}(ms)$	P_{IE}
15	0.195	117	0.805

tionship between MWF and IE GMT_2 across all white matter structures appears to be enhanced by the moderately strong correlation between these measurements in the individual structures of the CST and splenium of CC. These two were the only structures with a significant linear regression when structures were examined individually. The strongest relationship between IE GMT_2 and MWF was found when the average IE GMT_2 and average MWF were compared for each structure across subjects.

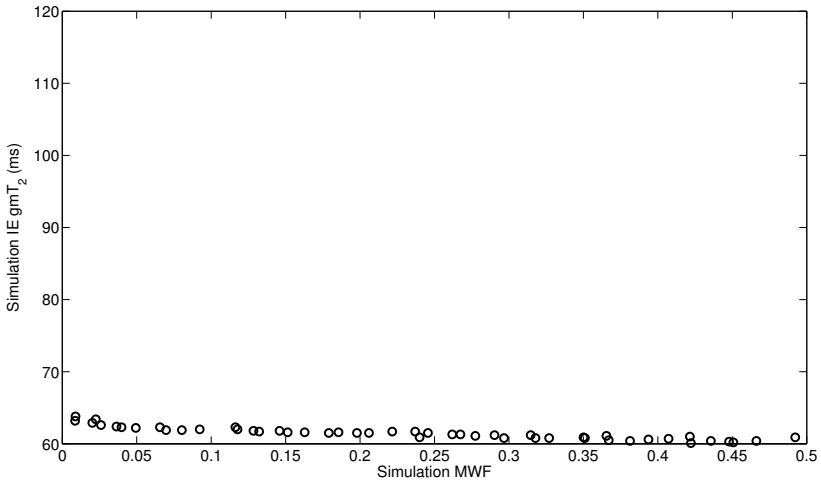

Figure 5.5: Output IE GMT_2 and MWF from NNLS simulation for n=100 trials and SNR=100

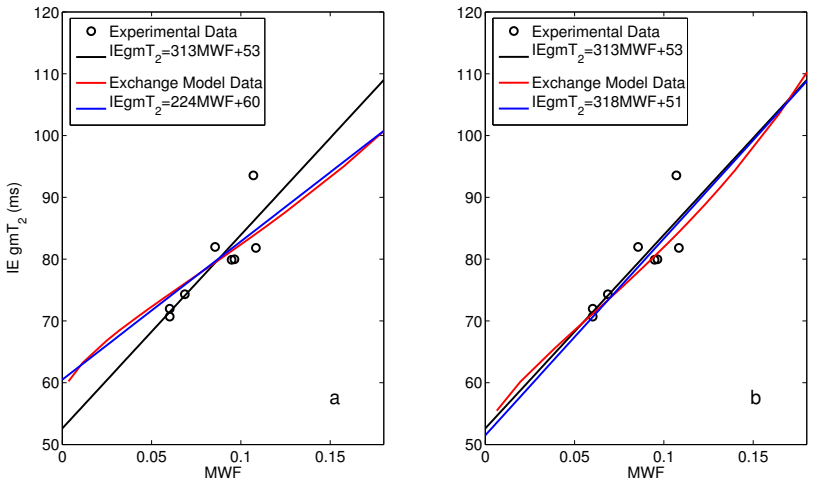

Figure 5.6: Relationship between IE GMT_2 and MWF resulting from the two-pool exchange model for a) the input parameter in Table 5.1 and b) the input parameters in Table 5.3

Two non-biological computational influences were examined and will be discussed here; regularization, and, NNLS fitting. As well, two biological influences that could responsible for the apparent positive linear relationship between IE GMT_2 and MWF will be discussed; increased extracellular water in higher MWF structures, and, decreased exchange in higher MWF structures.

Regularization can have an effect on the position of the T_2 distribution peaks, however, it is convention to include regularization to produce wider curves peaks rather than distinct spikes as these curves are more robust in the presence of noise. The relationship between IE GMT_2 and MWF does not appear to be the result of regularization, similar linear regression results were found for data from non-regularized and regularized T_2 distributions.

The positions of the T_2 peaks are influenced by the NNLS fitting program, especially if two water environments are close in T_2 time [59, 69]. This current study found that the NNLS fitting algorithm was not responsible for the relationship between MWF and IE GMT_2 across all structures. Rather a small gradual decrease is seen in the IE GMT_2 as MWF is increased, the algorithm appears to be pull the two peaks closer together.

However, according to Whittall [68] higher IE GMT_2 values were found to be associated with higher MWF data points using a different NNLS simulation. This simulation used a single input MWF and GMT_2 with the introduction of noise to produce a range of output MWF and corresponding output IE GMT_2 values. A white matter model of $M(t) = 0.2e^{\frac{-t}{20ms}} + 0.8e^{-\frac{t}{80ms}}$ with 1500 realizations of 1% Gaussian noise was used in a non-regularized NNLS calculation. Those results containing only two T_2 components were used to plot IE GMT_2 and MWF. The resultant fit had an equation given by $IEgmT2 = 58MWF + 68$. These results suggest the relationships seen in individual structures could be the result of NNLS and not an underlying biological factor. However, the high correlation between average IE GMT_2 and average MWF across all structures (see Figure 5.3) does not appear to be accounted for by NNLS because different structures give rise to different slopes (see Table 5.2).

Previous work by Whittall et al. [70] found a positive linear relationship between MWF and IE distribution width (W), a reflection of the variance in the T_2 distribution on a logarithmic scale. The IC and splenium of CC had significantly higher

IEW than all other structures examined; this suggested a greater inhomogeneity in the water environment of these structures [62]. A source of inhomogeneity is the myelin sheath itself, which separates water environments and restricts diffusion across the sheath [8]. In the previous chapter, the CST and splenium of CC were found to have the widest IE peaks and the largest amount of signal in the $25-40ms$ T_2 time range. It was proposed that this may arise from increased extracellular water in these two structures.

In fact, the relationship between MWF and IE GMT_2 could also be accounted for by increased extracellular water. We speculate that higher MWF structures have higher extracellular spaces and thus higher extracellular water. It is possible that larger thicker axons implying a higher MWF, could result in less axon packing and larger spaces in between, and thus increased extracellular water which would result in longer IE T_2 times. The CST is already known to have large axons with large clear spaces in between [73], however the amount of extracellular water has not been quantified and compared to other structures.

Exchange has been a subject of debate in MRI, specifically in T_1 and T_2 relaxation measurements [4, 9, 21, 25, 61]. Myelin is known to restrict diffusion across the sheaths [8], however, diffusion still occurs and may have an effect on the T_2 peaks. Two studies looked at exchange in rat spinal cord and found that smaller axons are affected by exchange due to the presence of thinner myelin sheaths; as a result the MWFs being measured may not be a proper representation of the actual myelin water content of the area [9, 21]. The presence of exchange blurs the separation of the water environments, and the measured T_2 times measured arise from combinations of different water environments. However, if exchange is in the slow regime than it has a negligible affect on the T_2 values and a multi-exponential T_2 fit can be used to separately measure the true T_2s of different water environments [10, 74].

The CST is known to have some of the largest axons in the brain [28, 29, 50], some of the other structures are known to have smaller axons [1, 73], the lack of exchange in the large axons and increase in exchange in the smaller axons could account for the changes in MWF and IE GMT_2 across all the structures [9, 10, 21, 61, 74]. The initial 'no-exchange' parameters input into the exchange model did not result in an acceptable fit to the experimental data. These initial input parameters

were taken from the experimental data and predicted to be the MWF and IE GMT_2 that would occur in the absence of exchange. However, the two-pool model could be made to fit by manipulating the input parameters. In order to make the exchange model fit, the input T_{2MW} was decreased to $15ms$, this caused the output predicted T_{2MW}s to be as low as $5ms$ corresponding to the lowest experimental IE GMT_2. T_2 times this low are difficult to measure experimentally because there are few TEs from which the low T_2 times are calculated and noise at these low TEs have a large effect on the extracted T_2 times. For example, a component with $T_2 = 5ms$ will only contribute $\sim 14\%$ of its total signal at our first TE time of $10ms$. In summary the exchange model can be made to fit, however the lower T_{2MW}s obtained from this model are unlikely to be measured reliably in experiment. As well, recent studies have found this is unlikely on timescales of these experiments [4, 25, 61]. However, exchange cannot eliminated as the mechanism for the correlation between IE GMT_2 and MWF.

Of the individual structures the CST had the strongest correlation between IE GMT_2 and MW. The CST has a wide distribution of sheath thicknesses [8, 28, 29, 50], resulting in a large range of exchange times from fast to slow which could account for the large range of MWFs and IE GMT_2s.

5.5 Conclusions

A relationship between IE GMT_2 and MWF was found when examined across all subjects and white matter structures. The strength of this relationship varied when individual structures were examined across subjects. Four different mechanisms were explored to explain this relationship, two had to do with the fitting algorithm and two were of biological origin.

The strong relationship across all structures and subjects could not be explained, however relationships within single structures may be the consequence of noise in T_2 distribution estimations.

The speculation was made that the higher MWF structures have increased extracellular water, which would give rise to increased IE GMT_2 in these structures. This could be responsible for the strong relationship between IE GMT_2 and MWF across all structures.

The two-pool exchange model for IE and MW can be made to fit experimental data. It can be made to fit the experimental data for average IE GMT_2 and average MWF. This model did, however, predict T_{2MW} that are short and difficult to measure reliably in the experimental data, these may be unrealistic T_{2MW} values.

Chapter 6

Conclusions

Long-T_2 times in healthy white matter structures have not been previously characterized using a multi-exponential T_2 technique with an extended echo sequence. Using a sequence with echoes extended to $1120ms$, it was found that the LT_2F was not appropriate for examining the CST. The T_2 distribution of the CST showed that the LT_2F was arising from signal in the IE peak and not from a separate water environment at longer T_2 times as previously thought.

The T_2 distribution of the CST was found different from the T_2 distributions of other white matter structures. The IE peak of the CST was broadened and extended to higher and lower T_2 times, which accounts for its bright appearance on T_2-weighted and MWF images respectively. The CST should not be examined using the conventional MWF T_2 time range of $5-40ms$, as this appears to result in an artificial increase in MWF. Based on these results, the CST does not appear to have the high level of myelin that was originally thought, but rather has a MWF similar to that of the splenium of CC and areas anterior and posterior to the CST.

The MWF and IE GMT_2 was found to be moderately correlated across all structures and subjects, and within the individual structures of the splenium of CC and CST. Four sources for this relationship were discussed, two non-biological and two biological. The real source of the relationship between IE GMT_2 and MWF across structures could not be determined, but could be the result of exchange between MW and IE or increases in extracellular water in high MWF structures. The relationship within structure may be the result of noise in the T_2 distribution analysis.

The complete nature of the T_2 signal in white matter is still not known, however, examining the T_2 distribution of structure more closely can provide additional information about the water environments of these structures.

6.1 Future Work

Increase in extracellular water in the CST and splenium of CC could account for the unique quantitative MR measures seen in these structures. The CST has already been found to have large clear extracellular spaces in comparison to areas posterior and anterior to it [73]. However, the amount of extracellular water in the CST has not been quantitatively compared to other white matter structures. The next step would be to determine the extracellular water using brain tissue samples and compare amount of extracellular water in different structures. If the extracellular water is responsible for the differences in T_2 distributions between structures, the structures with the narrower IE peaks should have a lower extracellular water content. The high MWF in the CST may be artifactual; this could also be examined histologically staining for myelin. If the staining intensity is similar between the CST and other structures such as and splenium of CC and anterior and posterior to the CST, than the previously found high MWF in the CST is most likely artifactual as proposed in Chapter 4.

The relationship between MWF and IE GMT_2 in the individual white matter structures may or may not be biological. The effects of NNLS on the movement of the IE peak need to be further examined by replicating the simulation completed by Whittall [68].

The work done here could be further extended to look at cases of ALS which give rise to pathological bright spots in the area of the CST on T_2-weighted images. T_2 distributions could provide better resolution in comparing these cases with healthy CST tissue, than earlier T_2 studies, which were not appropriate for examining separate water environments within a structure.

Bibliography

[1] F. Aboitiz, A. B. Scheibel, R. S. Fisher, and E. Zaidel. Fiber composition of the human corpus callosum. *Brain Research*, 598(1-2):143–153, Dec. 1992. ISSN 0006-8993. doi:16/0006-8993(92)90178-C. URL http://www.sciencedirect.com/science/article/pii/000689939290178C. → pages 34, 46

[2] B. A. Bell, M. A. Smith, D. M. Kean, C. N. McGhee, H. L. MacDonald, J. D. Miller, G. H. Barnett, J. L. Tocher, R. H. Douglas, and J. J. Best. Brain water measured by magnetic resonance imaging. correlation with direct estimation and changes after mannitol and dexamethasone. *Lancet*, 1(8524): 66–69, Jan. 1987. ISSN 0140-6736. URL http://www.ncbi.nlm.nih.gov/pubmed/2879175. PMID: 2879175. → pages 3

[3] T. A. Bjarnason and J. R. Mitchell. AnalyzeNNLS: magnetic resonance multiexponential decay image analysis. *Journal of Magnetic Resonance*, 206(2):200–204, Oct. 2010. ISSN 1090-7807. doi:16/j.jmr.2010.07.008. URL http://www.sciencedirect.com/science/article/pii/S1090780710002144. → pages 17, 28, 29

[4] T. A. Bjarnason, I. M. Vavasour, C. L. Chia, and A. L. MacKay. Characterization of the NMR behavior of white matter in bovine brain. *Magnetic Resonance in Medicine*, 54(5):1072–1081, Nov. 2005. ISSN 1522-2594. doi:10.1002/mrm.20680. URL http://onlinelibrary.wiley.com/doi/10.1002/mrm.20680/abstract. → pages 34, 39, 46, 47

[5] F. Bloch. Nuclear induction. *Phys. Rev.*, 70:460–474, Oct 1946. doi:10.1103/PhysRev.70.460. URL http://link.aps.org/doi/10.1103/PhysRev.70.460. → pages 7

[6] N. Bloembergen, E. M. Purcell, and R. V. Pound. Relaxation effects in nuclear magnetic resonance absorption. *Physical Review*, 73(7):679, Apr.

1948. doi:10.1103/PhysRev.73.679. URL http://link.aps.org/doi/10.1103/PhysRev.73.679. → pages 8

[7] M. Bloom, K. T. Holmes, C. E. Mountford, and P. G. Williams. Complete proton magnetic resonance in whole cells. *Journal of Magnetic Resonance (1969)*, 69(1):73–91, Aug. 1986. ISSN 0022-2364. doi:10.1016/0022-2364(86)90219-2. URL http://www.sciencedirect.com/science/article/pii/0022236486902192. → pages 2

[8] T. L. Chenevert, J. A. Brunberg, and J. G. Pipe. Anisotropic diffusion in human white matter: demonstration with MR techniques in vivo. *Radiology*, 177(2):401–405, Nov. 1990. ISSN 0033-8419. URL http://www.ncbi.nlm.nih.gov/pubmed/2217776. PMID: 2217776. → pages 46, 47

[9] A. N. Dula, D. F. Gochberg, H. L. Valentine, W. M. Valentine, and M. D. Does. Multiexponential t2, magnetization transfer, and quantitative histology in white matter tracts of rat spinal cord. *Magnetic Resonance in Medicine: Official Journal of the Society of Magnetic Resonance in Medicine / Society of Magnetic Resonance in Medicine*, 63(4):902–909, Apr. 2010. ISSN 1522-2594. doi:10.1002/mrm.22267. URL http://www.ncbi.nlm.nih.gov/pubmed/20373391. PMID: 20373391. → pages 34, 35, 46

[10] H. T. Edzes and E. T. Samulski. The measurement of cross-relaxation effects in the proton NMR spin-lattice relaxation of water in biological systems: Hydrated collagen and muscle. *Journal of Magnetic Resonance (1969)*, 31 (2):207–229, Aug. 1978. ISSN 0022-2364. doi:16/0022-2364(78)90185-3. URL http://www.sciencedirect.com/science/article/pii/0022236478901853. → pages 11, 39, 46

[11] P. P. Fatouros and A. Marmarou. Use of magnetic resonance imaging for in vivo measurements of water content in human brain: method and normal values. *Journal of Neurosurgery*, 90(1):109–115, Jan. 1999. ISSN 0022-3085. doi:10.3171/jns.1999.90.1.0109. URL http://www.ncbi.nlm.nih.gov/pubmed/10413163. PMID: 10413163. → pages 3

[12] J. B. Finean. Electron microscope and x-ray diffraction studies of the effects of dehydration on the structure of nerve myelin. *The Journal of Biophysical*

and Biochemical Cytology, 8(1):13 –29, 1960. doi:10.1083/jcb.8.1.13. URL http://jcb.rupress.org/content/8/1/13.abstract. → pages 2

[13] H. W. Fischer, P. A. Rinck, Y. Van Haverbeke, and R. N. Muller. Nuclear relaxation of human brain gray and white matter: analysis of field dependence and implications for MRI. *Magnetic Resonance in Medicine: Official Journal of the Society of Magnetic Resonance in Medicine / Society of Magnetic Resonance in Medicine*, 16(2):317–334, Nov. 1990. ISSN 0740-3194. URL http://www.ncbi.nlm.nih.gov/pubmed/2266850. PMID: 2266850. → pages 2, 4

[14] D. P. Friedman and L. M. Tartaglino. Amyotrophic lateral sclerosis: hyperintensity of the corticospinal tracts on MR images of the spinal cord. *American Journal of Roentgenology*, 160(3):604 –606, Mar. 1993. URL http://www.ajronline.org/content/160/3/604.short. → pages 25

[15] P. J. Gareau, B. K. Rutt, C. V. Bowen, S. J. Karlik, and J. R. Mitchell. In vivo measurements of multi-component t2 relaxation behaviour in guinea pig brain. *Magnetic Resonance Imaging*, 17(9):1319–1325, Nov. 1999. ISSN 0730-725X. URL http://www.ncbi.nlm.nih.gov/pubmed/10576717. PMID: 10576717. → pages 4, 26

[16] P. J. Gareau, B. K. Rutt, S. J. Karlik, and J. R. Mitchell. Magnetization transfer and multicomponent t2 relaxation measurements with histopathologic correlation in an experimental model of MS. *Journal of Magnetic Resonance Imaging: JMRI*, 11(6):586–595, June 2000. ISSN 1053-1807. URL http://www.ncbi.nlm.nih.gov/pubmed/10862056. PMID: 10862056. → pages 4, 26

[17] M. Goldman and L. Shen. Spin-Spin relaxation in LaF_3. *Physical Review*, 144(1):321, Apr. 1966. doi:10.1103/PhysRev.144.321. URL http://link.aps.org/doi/10.1103/PhysRev.144.321. → pages 39

[18] D. S. Goodin, H. A. Rowley, and R. K. Olney. Magnetic resonance imaging in amyotrophic lateral sclerosis. *Annals of Neurology*, 23(4):418–420, Apr. 1988. ISSN 1531-8249. doi:10.1002/ana.410230424. URL http://onlinelibrary.wiley.com/doi/10.1002/ana.410230424/abstract. → pages 25

[19] M. D. Greenberg. *Differential Equations and Linear Algebra*. Prentice Hall, 1 edition, Dec. 2000. ISBN 013011118X. → pages 12

[20] E. M. Haacke, R. W. Brown, M. R. Thompson, and R. Venkatesan. *Magnetic Resonance Imaging: Physical Principles and Sequence Design*. Wiley-Liss, 1st edition, June 1999. ISBN 0471351288. → pages 6, 7, 8, 9

[21] K. D. Harkins, A. N. Dula, and M. D. Does. Effect of intercompartmental water exchange on the apparent myelin water fraction in multiexponential t(2) measurements of rat spinal cord. *Magnetic Resonance in Medicine: Official Journal of the Society of Magnetic Resonance in Medicine / Society of Magnetic Resonance in Medicine*, June 2011. ISSN 1522-2594. doi:10.1002/mrm.23053. URL http://www.ncbi.nlm.nih.gov/pubmed/21713984. PMID: 21713984. → pages 34, 35, 46

[22] P. Herv, E. F. Cox, A. K. Lotfipour, O. E. Mougin, R. W. Bowtell, P. A. Gowland, and T. Paus. Structural properties of the corticospinal tract in the human brain: a magnetic resonance imaging study at 7 tesla. *Brain Structure & Function*, 216(3):255–262, Sept. 2011. ISSN 1863-2661. doi:10.1007/s00429-011-0306-0. URL http://www.ncbi.nlm.nih.gov/pubmed/21409416. PMID: 21409416. → pages 26, 27, 33, 34

[23] E. Hofmann, G. Ochs, A. Pelzl, and M. Warmuth-Metz. The corticospinal tract in amyotrophic lateral sclerosis: an MRI study. *Neuroradiology*, 40(2): 71–75, Feb. 1998. ISSN 0028-3940. URL http://www.ncbi.nlm.nih.gov/pubmed/9541915. PMID: 9541915. → pages 25

[24] S. H. Jang. A review of corticospinal tract location at corona radiata and posterior limb of the internal capsule in human brain. *NeuroRehabilitation*, 24(3):279–283, 2009. ISSN 1053-8135. doi:10.3233/NRE-2009-0479. URL http://www.ncbi.nlm.nih.gov/pubmed/19458436. PMID: 19458436. → pages 15, 26

[25] S. Kalantari, C. Laule, T. A. Bjarnason, I. M. Vavasour, and A. L. Mackay. Insight into in vivo magnetization exchange in human white matter regions. *Magnetic Resonance in Medicine: Official Journal of the Society of Magnetic Resonance in Medicine / Society of Magnetic Resonance in Medicine*, Mar. 2011. ISSN 1522-2594. doi:10.1002/mrm.22873. URL http://www.ncbi.nlm.nih.gov/pubmed/21381107. PMID: 21381107. → pages 35, 46, 47

[26] Y. Kaneoke, M. Furuse, S. Inao, K. Saso, K. Yoshida, Y. Motegi, M. Mizuno, and A. Izawa. Spin-lattice relaxation times of bound water–its determination and implications for tissue discrimination. *Magnetic Resonance Imaging*, 5(6):415–420, 1987. ISSN 0730-725X. URL http://www.ncbi.nlm.nih.gov/pubmed/3431351. PMID: 3431351. → pages 3

[27] J. Keller, J. Vymazal, P. Ridzo, R. Rusina, P. Kulit'k, H. Malkov, A. M. Rulseh, O. Keller, and R. Jech. Quantitative brain MR imaging in amyotrophic lateral sclerosis. *Magma (New York, N.Y.)*, 24(2):67–76, Apr. 2011. ISSN 0968-5243. doi:10.1007/s10334-010-0237-4. URL http://www.ncbi.nlm.nih.gov/pubmed/21404113. PMID: 21404113. → pages 25

[28] A. M. Lassek. The human pyramidal tract. IV. a study of the mature, myelinated fibers of the pyramid. *The Journal of Comparative Neurology*, 76(2):217–225, Apr. 1942. ISSN 1096-9861. doi:10.1002/cne.900760203. URL http://onlinelibrary.wiley.com/doi/10.1002/cne.900760203/abstract. → pages 26, 46, 47

[29] A. M. Lassek and G. L. Rasmussen. The human pyramidal tract: A fiber and numerical analysis. *Arch Neurol Psychiatry*, 42(5):872–876, Nov. 1939. doi:⟨p⟩10.1001/archneurpsyc.1939.02270230094007⟨/p⟩. URL http://archneurpsyc.ama-assn.org. → pages 26, 46, 47

[30] C. Laule, I. M. Vavasour, G. R. W. Moore, J. Oger, D. K. B. Li, D. W. Paty, and A. L. MacKay. Water content and myelin water fraction in multiple sclerosis. *Journal of Neurology*, 251:284–293, Mar. 2004. ISSN 0340-5354, 1432-1459. doi:10.1007/s00415-004-0306-6. URL http://www.springerlink.com/content/9q6wnv7gulwqp5pr/. → pages 4

[31] C. Laule, E. Leung, D. K. Li, A. L. Traboulsee, D. W. Paty, A. L. MacKay, and G. R. Moore. Myelin water imaging in multiple sclerosis: quantitative correlations with histopathology. *Multiple Sclerosis*, 12(6):747 –753, Nov. 2006. doi:10.1177/1352458506070928. URL http://msj.sagepub.com/content/12/6/747.abstract. → pages 4, 26

[32] C. Laule, S. H. Kolind, T. A. Bjarnason, D. K. B. Li, and A. L. MacKay. In vivo multiecho t2 relaxation measurements using variable TR to decrease scan time. *Magnetic Resonance Imaging*, 25(6):834–839, July 2007. ISSN 0730-725X. doi:10.1016/j.mri.2007.02.016. URL http://www.ncbi.nlm.nih.gov/pubmed/17482413. PMID: 17482413. → pages 1, 17

[33] C. Laule, I. M. Vavasour, S. H. Kolind, D. K. Li, T. L. Traboulsee, G. W. Moore, and A. L. MacKay. Magnetic resonance imaging of myelin. *Neurotherapeutics*, 4(3):460–484, July 2007. ISSN 1933-7213. doi:10.1016/j.nurt.2007.05.004. URL http://www.sciencedirect.com/science/article/pii/S1933721307000888. → pages 2

[34] C. Laule, I. M. Vavasour, S. H. Kolind, A. L. Traboulsee, G. R. W. Moore, D. K. B. Li, and A. L. MacKay. Long t2 water in multiple sclerosis: What else can we learn from multi-echo t2 relaxation? *Journal of Neurology*, 254 (11):1579–1587, Sept. 2007. ISSN 0340-5354. doi:10.1007/s00415-007-0595-7. URL http://www.springerlink.com/content/31870831221648j2/. → pages 3, 4, 15, 26

[35] C. Laule, I. M. Vavasour, B. Mdler, S. H. Kolind, S. M. Sirrs, E. E. Brief, A. L. Traboulsee, G. R. W. Moore, D. K. B. Li, and A. L. MacKay. MR evidence of long t2 water in pathological white matter. *Journal of Magnetic Resonance Imaging: JMRI*, 26(4):1117–1121, Oct. 2007. ISSN 1053-1807. doi:10.1002/jmri.21132. URL http://www.ncbi.nlm.nih.gov/pubmed/17896375. PMID: 17896375. → pages 1, 3, 4, 15, 16, 24, 26, 33, 34

[36] C. Laule, P. Kozlowski, E. Leung, D. K. Li, A. L. MacKay, and G. W. Moore. Myelin water imaging of multiple sclerosis at 7 t: Correlations with histopathology. *NeuroImage*, 40(4):1575–1580, May 2008. ISSN 1053-8119. doi:10.1016/j.neuroimage.2007.12.008. URL http://www.sciencedirect.com/science/article/pii/S1053811907010981. → pages 4, 26

[37] C. L. Lawson and R. J. Hanson. *Solving Least Squares Problems*. Society for Industrial Mathematics, Jan. 1987. ISBN 0898713560. → pages 10, 17, 28

[38] A. MacKay, K. Whittall, J. Adler, D. Li, D. Paty, and D. Graeb. In vivo visualization of myelin water in brain by magnetic resonance. *Magnetic Resonance in Medicine: Official Journal of the Society of Magnetic Resonance in Medicine / Society of Magnetic Resonance in Medicine*, 31(6): 673–677, June 1994. ISSN 0740-3194. URL http://www.ncbi.nlm.nih.gov/pubmed/8057820. PMID: 8057820. → pages 2, 3, 4, 10, 26

[39] A. MacKay, C. Laule, I. Vavasour, T. Bjarnason, S. Kolind, and B. Mdler. Insights into brain microstructure from the t2 distribution. *Magnetic Resonance Imaging*, 24(4):515–525, May 2006. ISSN 0730-725X. doi:16/j.mri.2005.12.037. URL http://www.sciencedirect.com/science/article/pii/S0730725X06000518. → pages 3, 10

[40] A. MacKay, I. Vavasour, A. Rauscher, S. Kolind, B. Mdler, G. Moore, A. Traboulsee, D. Li, and C. Laule. MR relaxation in multiple sclerosis. *Neuroimaging Clinics of North America*, 19(1):1–26, Feb. 2009. ISSN 1052-5149. doi:16/j.nic.2008.09.007. URL http://www.sciencedirect.com/science/article/pii/S1052514908000932. → pages 1, 2, 3, 4, 8, 10, 26, 33

[41] S. Meiboom and D. Gill. Modified Spin-Echo method for measuring nuclear relaxation times. *Review of Scientific Instruments*, 29:688, 1958. ISSN 00346748. doi:10.1063/1.1716296. URL http://link.aip.org/link/RSINAK/v29/i8/p688/s1&Agg=doi. → pages 8

[42] R. S. Menon and P. S. Allen. Application of continuous relaxation time distributions to the fitting of data from model systems and excised tissue. *Magnetic Resonance in Medicine: Official Journal of the Society of Magnetic Resonance in Medicine / Society of Magnetic Resonance in Medicine*, 20(2):214–227, Aug. 1991. ISSN 0740-3194. URL http://www.ncbi.nlm.nih.gov/pubmed/1775048. PMID: 1775048. → pages 4, 26

[43] R. S. Menon, M. S. Rusinko, and P. S. Allen. Multiexponential proton relaxation in model cellular systems. *Magnetic Resonance in Medicine*, 20 (2):196–213, Aug. 1991. ISSN 1522-2594. doi:10.1002/mrm.1910200204. URL http://onlinelibrary.wiley.com/doi/10.1002/mrm.1910200204/abstract. → pages 26

[44] R. S. Menon, M. S. Rusinko, and P. S. Allen. Proton relaxation studies of water compartmentalization in a model neurological system. *Magnetic Resonance in Medicine: Official Journal of the Society of Magnetic Resonance in Medicine / Society of Magnetic Resonance in Medicine*, 28(2): 264–274, Dec. 1992. ISSN 0740-3194. URL http://www.ncbi.nlm.nih.gov/pubmed/1281258. PMID: 1281258. → pages 4, 26

[45] C. Moler and C. V. Loan. Nineteen dubious ways to compute the exponential of a matrix, Twenty-Five years later. *SIAM Review*, 45(1):3–49, Mar. 2003. ISSN 0036-1445. URL http://www.jstor.org/stable/25054364. ArticleType: research-article / Full publication date: Mar., 2003 / Copyright 2003 Society for Industrial and Applied Mathematics. → pages 12

[46] G. W. Moore, E. Leung, A. MacKay, I. Vavasour, K. Whittall, K. Cover, D. B. Li, S. Hashimoto, J. Oger, T. Sprinkle, and D. Paty. A pathology-MRI study of the short-T2 component in formalin-fixed multiple sclerosis brain. *Neurology*, 55(10):1506 –1510, Nov. 2000. URL http://www.neurology.org/content/55/10/1506.abstract. → pages 4, 26

[47] P. W. Nathan and M. C. Smith. Long descending tracts in man. i. review of present knowledge. *Brain: A Journal of Neurology*, 78(2):248–303, 1955. ISSN 0006-8950. URL http://www.ncbi.nlm.nih.gov/pubmed/13239911. PMID: 13239911. → pages 26

[48] W. Norton and W. Cammer. Isolation and characterization of myelin. In P. Morell, editor, *Myelin*, pages 147–195. Plenum Press, New York, 2^{nd} edition, 1984. → pages 2

[49] W. T. Norton, S. E. Poduslo, and K. Suzuki. Subacute sclerosing leukoencephalitis. II. chemical studies including abnormal myelin and an abnormal ganglioside pattern. *Journal of Neuropathology and Experimental Neurology*, 25(4):582–597, Oct. 1966. ISSN 0022-3069. URL http://www.ncbi.nlm.nih.gov/pubmed/5922554. PMID: 5922554. → pages 3

[50] A. Parent. *Carpenter's human neuroanatomy*. Williams & Wilkins, Baltimore, 9th ed. edition, 1996. ISBN 9780683067521. → pages 26, 28, 46, 47

[51] R. Quarles, W. Macklin, and P. Morell. Myelin formation, structure and biochemistry. In G. Siegel, R. Albers, S. Brady, and D. Price, editors, *Basic neurochemistry: molecular, cellular, and medical aspects*, pages 51–71. Academic Press, 2006. → pages 2

[52] C. Raine. Morphology of myelin and myelination. In P. Morell, editor, *Myelin*, pages 1–50. Plenum Press, New York, 2^{nd} edition, 1984. → pages 2

[53] D. S. Reich, S. A. Smith, C. K. Jones, K. M. Zackowski, P. C. van Zijl, P. A. Calabresi, and S. Mori. Quantitative characterization of the corticospinal tract at 3T. *AJNR. American Journal of Neuroradiology*, 27(10):2168–2178, Dec. 2006. ISSN 0195-6108. URL

http://www.ncbi.nlm.nih.gov/pubmed/17110689. PMID: 17110689. → pages 26, 33

[54] J. Ritchie. Physiological basis of conduction in myelinated nerve fibers. In P. Morell, editor, *Myelin*, pages 117–145. Plenum Press, New York, 2nd edition, 1984. → pages 2

[55] W. A. H. Rushton. A theory of the effects of fibre size in medullated nerve. *The Journal of Physiology*, 115(1):101 –122, 1951. URL http://jp.physoc.org/content/115/1/101.short. → pages 2, 26

[56] J. L. Schepps and K. R. Foster. The UHF and microwave dielectric properties of normal and tumour tissues: variation in dielectric properties with tissue water content. *Physics in Medicine and Biology*, 25(6): 1149–1159, Nov. 1980. ISSN 0031-9155. URL http://www.ncbi.nlm.nih.gov/pubmed/7208627. PMID: 7208627. → pages 3

[57] L. Sherwood and R. Kell. *Human Physiology: From Cells to Systems*. Nelson Education Ltd., 2010. ISBN 0898713560. → pages 2

[58] S. M. Sirrs, C. Laule, B. Mdler, E. E. Brief, S. A. Tahir, C. Bishop, and A. L. MacKay. Normal-appearing white matter in patients with phenylketonuria: water content, myelin water fraction, and metabolite concentrations. *Radiology*, 242(1):236–243, Jan. 2007. ISSN 0033-8419. doi:10.1148/radiol.2421051758. URL http://www.ncbi.nlm.nih.gov/pubmed/17185670. PMID: 17185670. → pages iv, 16, 17, 26

[59] M. G. Skinner, S. H. Kolind, and A. L. MacKay. The effect of varying echo spacing within a multiecho acquisition: better characterization of long t2 components. *Magnetic Resonance Imaging*, 25(6):840–847, July 2007. ISSN 0730-725X. doi:10.1016/j.mri.2006.09.046. URL http://www.ncbi.nlm.nih.gov/pubmed/17418518. PMID: 17418518. → pages 4, 17, 27, 45

[60] C. P. Slichter. *Principles of Magnetic Resonance (Springer Series in Solid-State Sciences)*. Springer, Mar. 1996. ISBN 3540501576. → pages 6, 7, 8, 9

[61] G. J. Stanisz, A. Kecojevic, M. J. Bronskill, and R. M. Henkelman. Characterizing white matter with magnetization transfer and t(2). *Magnetic Resonance in Medicine: Official Journal of the Society of Magnetic Resonance in Medicine / Society of Magnetic Resonance in Medicine*, 42(6):

1128–1136, Dec. 1999. ISSN 0740-3194. URL http://www.ncbi.nlm.nih.gov/pubmed/10571935. PMID: 10571935. → pages 34, 46, 47

[62] W. A. Stewart, A. L. MacKay, K. P. Whittall, G. R. Moore, and D. W. Paty. Spin-spin relaxation in experimental allergic encephalomyelitis. analysis of CPMG data using a non-linear least squares method and linear inverse theory. *Magnetic Resonance in Medicine: Official Journal of the Society of Magnetic Resonance in Medicine / Society of Magnetic Resonance in Medicine*, 29(6):767–775, June 1993. ISSN 0740-3194. URL http://www.ncbi.nlm.nih.gov/pubmed/8350719. PMID: 8350719. → pages 3, 4, 26, 27, 46

[63] H. Takagi, K. Shapiro, A. Marmarou, and H. Wisoff. Micrograviметric analysis of human brain tissue: correlation with computerized tomography scanning. *Journal of Neurosurgery*, 54(6):797–801, June 1981. ISSN 0022-3085. doi:10.3171/jns.1981.54.6.0797. URL http://www.ncbi.nlm.nih.gov/pubmed/6264051. PMID: 6264051. → pages 3

[64] P. Tofts. Pd: Proton density of tissue water. In P. Tofts, editor, *Quantitative MRI of the Brain: measuring changes caused by disease*, pages 85–109. John Wiley and Sons, Ltd., England, 2003. → pages

[65] W. W. Tourtellotte and J. A. Parker. Some spaces and barriers in postmortem multiple sclerosis. *Progress in Brain Research*, 29:493–525, 1968. ISSN 0079-6123. doi:10.1016/S0079-6123(08)64178-3. URL http://www.ncbi.nlm.nih.gov/pubmed/5735306. PMID: 5735306. → pages 3

[66] V. Vasilescu, E. Katona, V. Simplceanu, and D. Demco. Water compartments in the myelinated nerve. III. pulsed NMR results. *Experientia*, 34(11):1443–1444, Nov. 1978. ISSN 0014-4754. URL http://www.ncbi.nlm.nih.gov/pubmed/309823. PMID: 309823. → pages 4

[67] S. Webb, C. A. Munro, R. Midha, and G. J. Stanisz. Is multicomponent t2 a good measure of myelin content in peripheral nerve? *Magnetic Resonance in Medicine: Official Journal of the Society of Magnetic Resonance in Medicine / Society of Magnetic Resonance in Medicine*, 49(4):638–645, Apr. 2003. ISSN 0740-3194. doi:10.1002/mrm.10411. URL http://www.ncbi.nlm.nih.gov/pubmed/12652534. PMID: 12652534. → pages 4, 26

[68] K. Whittall. Does an increased mwf imply an increased main water t2? Private communication, 2011. → pages 45, 50

[69] K. P. Whittall and A. L. MacKay. Quantitative interpretation of NMR relaxation data. *Journal of Magnetic Resonance (1969)*, 84(1):134–152, Aug. 1989. ISSN 0022-2364. doi:16/0022-2364(89)90011-5. URL http://www.sciencedirect.com/science/article/pii/0022236489900115. → pages 10, 11, 17, 29, 37, 45

[70] K. P. Whittall, A. L. MacKay, D. A. Graeb, R. A. Nugent, D. K. Li, and D. W. Paty. In vivo measurement of t2 distributions and water contents in normal human brain. *Magnetic Resonance in Medicine: Official Journal of the Society of Magnetic Resonance in Medicine / Society of Magnetic Resonance in Medicine*, 37(1):34–43, Jan. 1997. ISSN 0740-3194. URL http://www.ncbi.nlm.nih.gov/pubmed/8978630. PMID: 8978630. → pages 3, 4, 15, 23, 26, 27, 33, 34, 36, 45

[71] K. P. Whittall, A. L. MacKay, and D. K. Li. Are mono-exponential fits to a few echoes sufficient to determine t2 relaxation for in vivo human brain? *Magnetic Resonance in Medicine: Official Journal of the Society of Magnetic Resonance in Medicine / Society of Magnetic Resonance in Medicine*, 41(6):1255–1257, June 1999. ISSN 0740-3194. URL http://www.ncbi.nlm.nih.gov/pubmed/10371459. PMID: 10371459. → pages 27

[72] Q. Xiang. Physics 542: Magnetic resonance imaging [lecture notes]. Vancouver, Canada: University of British Columbia, Department of Physics and Astronomy. → pages 7, 8, 9

[73] A. Yagishita, I. Nakano, M. Oda, and A. Hirano. Location of the corticospinal tract in the internal capsule at MR imaging. *Radiology*, 191(2): 455 –460, May 1994. URL http://radiology.rsna.org/content/191/2/455.abstract. → pages 15, 17, 25, 26, 33, 34, 46, 50

[74] J. Zimmerman and W. Brittin. Nuclear magnetic resonance studies in multiple phase systems: Lifetime of a water molecule in an adsorbing phase on silica gel. *The Journal of Physical Chemistry*, 61(10):1328–1333, Oct. 1957. URL http://dx.doi.org/10.1021/j150556a015. → pages 11, 34, 39, 46